Deformation and initial breakup morphology of viscous emulsion drops in isotropic homogeneous turbulence with relevance for emulsification devices

Chemical Engineering Science 253 (2022) 117599

Contents lists available at ScienceDirect

Chemical Engineering Science

journal homepage: www.elsevier.com/locate/ces

Deformation and initial breakup morphology of viscous emulsion drops in isotropic homogeneous turbulence with relevance for emulsification devices

Andreas Håkansson [a,*], Luca Brandt [b,c]

[a] Department of Food Technology, Engineering and Nutrition, LTH at Lund University, Lund, Sweden
[b] Flow Centre, Department of Engineering Mechanics, Royal Institute of Technology (KTH), Stockholm, Sweden
[c] Department of Energy and Process Engineering, Norwegian University of Science and Technology (NTNU), Trondheim, Norway

HIGHLIGHTS

- Breakup of viscous drops in HPH-similar conditions was studied with DNS.
- Deformation is in a single (multiple) direction(s) for small (large) drops.
- The lower the We, the more likely a drop is to enter an oscillatory phase.
- The higher the We, the more likely a drop is to enter critical deformation/breakup.
- Breakup occurs deterministically once a sufficiently thin neck has formed locally.

GRAPHICAL ABSTRACT

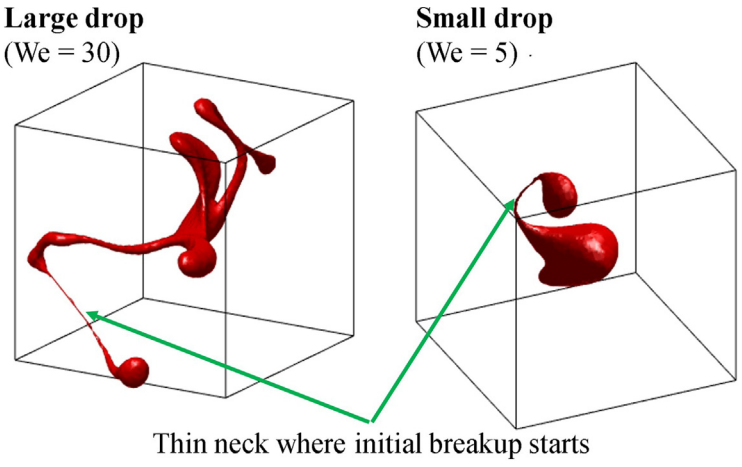

ARTICLE INFO

Article history:
Received 12 January 2022
Received in revised form 23 February 2022
Accepted 6 March 2022
Available online 10 March 2022

Keywords:
Emulsification
DNS
Drop breakup
Fragmentation
Turbulence
High-pressure homogenizer

ABSTRACT

This study uses numerical experiments to investigate initial breakup morphology for conditions similar to those experienced in an emulsification device (e.g., a high-pressure homogenizer) (Re_λ = 33, We = 1–30, μ_D/μ_C = 22, ρ_D/ρ_C = 0.9, D/η = 22). Results show breakup consisting of two phases: and 'oscillatory phase' where the drops are periodically deforming and relaxing, followed by a 'critical deformation phase' where the drop deforms continuously until initial breakup. Large drops (We $\geq$ 13) go directly to the breakup phase and are highly deformed in multiple direction before bursting. Smaller drops (3 $\leq$ We $\leq$ 5) are less likely to go directly to the critical deformation phase and more likely to never reach it before exiting the device. These drops break by the formation of a single filament, creating two large fragments and a number of smaller satellites. Several turbulent structures contribute to critical deformation.

* Corresponding author.
E-mail addresses: andreas@a-hakansson.se, andreas.hakansson@food.lth.se (A. Håkansson).

https://doi.org/10.1016/j.ces.2022.117599
0009-2509/

Nomenclature

Abbreviations

DNS	Direct numerical simulation
HPH	High-pressure homogenizer
LES	Large eddy simulation
RMS	Root mean square
TKE	Turbulent kinetic energy
VOF	Volume of fluid

Symbols

A, A_0	Interfacial area (and initial interfacial area), m^2
C_1, C_2	Constants in Eq. (1)
D	Drop diameter, m
D_0	Initial drop diameter, m
D_{max}	Maximum drop diameter, m
f_2	Characteristic frequency of the drop, s^{-1}
h	Gap height, m
L	Integral length-scale, m
L_{box}	Edge length of the simulation cube
N	Number of computational cells (in each dimension)
Q	Second invariant of the velocity tensor, s^{-1}
Re_λ	Taylor-scale Reynolds number
T	Time spent in the turbulent region, s
t	Time, s
t_B	Time of initial break (injection to breakup), s
t_B^*	Corrected initial breakup time, s
u'	RMS velocity, m
U_g	HPH gap exit velocity, m s^{-1}
We	Weber number (Eq. (3))

Greek

α	VOF of dispersed phase
β_2	Dampening rate of the drop, s
γ	Interfacial tension, N m^{-1}
ε	Dissipation rate of TKE, m^2 s^{-3}
η	Kolmogorov length-scale, m
λ	Taylor length-scale, m
μ_C	Continuous phase dynamic viscosity, Pa s
μ_D	Disperse phase dynamic viscosity, Pa s
ν_C	Continuous phase kinematic viscosity, m^2 s^{-1}
ξ	Dimensionless dampening rate
ρ_C	Continuous phase density, kg m^{-3}
τ_η	Kolmogorov time-scale, s

1. Introduction

Emulsification is a commonly used unit operation, aimed at producing a stable homogenous dispersion of two immiscible fluids (McClements, 2016; Tadros, 2013). Applications range from food, to pharmaceutical and general chemical processing. Products with a low to intermediate continuous phase viscosity are typically produced using (valve) high-pressure homogenizers (HPHs) (Håkansson, 2019; Schultz et al., 2004). Homogenization of (cow) milk, for increased physical stability, is the single largest application. The disperse to continuous phase viscosity ratio is typically high in these applications ($\mu_D/\mu_C \sim 20$) due to the high dynamic viscosities of food grade fats and vegetable oils (Phipps, 1985).

The HPH operates in a continuous mode and allows for scale-up, but is relatively inefficient from a thermodynamic perspective (Mohr, 1987). Consequently, there is a large interest in increasing the fundamental understanding of drop breakup in HPHs to further optimise device design and operation.

Experimental investigations have showed how the narrow valve ($h \sim 10$–100 μm) gives rise to an acceleration of the fluid upstream of the gap and the development of an intense high velocity turbulent jet downstream of the gap ($U_g \sim 100$ m/s) (Håkansson et al., 2011; Innings and Trägårdh, 2007; Kelemen et al., 2015; Mutsch et al., 2021). Breakup visualizations with high-speed imaging have revealed that drops are deformed and then break in the turbulent jet created downstream of the gap (Innings and Trägårdh, 2007; Innings et al., 2011; Kelemen et al., 2015; Mutsch et al., 2021; Preiss et al., 2021). Comparing breakup visualizations to turbulence statistics, leads to the conclusion that turbulent interactions are responsible for breaking the drop (Håkansson et al., 2011; Håkansson, 2018).

Direct numerical simulations (DNS) have been used to investigate a turbulent jet in a domain similar to a HPH, suggesting that the turbulent structures behave relatively ideally on the scales postulated to be responsible for turbulent inertial or viscous breakup; i.e., the energy spectra and the relation between second-order structure functions and dissipation rate of turbulent kinetic energy (TKE) are fairly similar to that of a homogenous, isotropic turbulent flow (Olad et al., 2021a, 2021b).

The growing number of high-quality experimental single drop breakup visualizations have greatly added to the mechanistic understanding of emulsification. This applies to both idealized turbulent flows (Andersson and Andersson, 2006; Eastwood et al., 2004; Herø et al., 2020; Martínez-Bazán et al., 1999; Masuk et al., 2021; Risso and Fabre, 1998; Vejražka et al., 2018) and more specific studies of breakup in emulsification devices (Ashar et al., 2018; Galinat et al., 2007; Innings et al., 2011; Kelemen et al., 2015; Maaß and Kraume, 2012; Mutsch et al., 2021; Preiss et al., 2021; Solsvik and Jakobsen, 2015). However, single drop breakup visualizations have limitations. Firstly, the experimental conditions in itself sets constraints, i.e., requiring scaling of the geometry to slow down the dynamics to the camera frame rate, and often relying on a 2D projection when studying the drop details (Bisten and Schuchmann, 2016; Håkansson, 2020). Secondly, the visualization results are limited in terms of time resolution, and typically only provide a few images per breakup event, making it difficult to fully visualize how the morphology evolves during the whole process. Thirdly, it remains challenging to measure both the drop morphology and the instantaneous turbulent field in an experimental setting, which makes it difficult to study direct interactions, local in space and time, using these techniques (see Masuk et al., 2021 for a recent exception).

Numerical experiments, where the turbulence is described using a model-free DNS and the drop morphology is described by a high-resolution volume of fluid (VOF) scheme, has emerged as a complementary method to study drop deformation and breakup from a mechanistic perspective. A comprehensive review of methodology and main findings is available elsewhere (Elghobashi, 2019) but a brief look at some of these previous contributions will prove informative:.

One branch of numerical breakup investigations has focused on how a large number of drops interact with turbulence and how the drop size distribution evolves over time when subjected to a turbulent flow. Skartlien et al. (2013) studied the evolution of the drop size distribution and maximum drop size of an emulsion (including a model for a mobile surfactant) in a forced isotropic homogenous turbulence. They found good agreement with the Kolmogorov-Hinze theory. Scarbolo et al. (2015) and later Rosti et al. (2019)

extended these investigations into channel and shear turbulence respectively. Scarbolo et al. (2015) studied a swarm of low viscosity ratio emulsion drops (μ_D/μ_C = 1.0), injected into a channel flow, and concluded on a difference in breakup dominated (We > 1) and coalescence dominated (We < 1) emulsification. More recent numerical investigations show the emulsification process going through an alternating dominance of breakup and coalescence as time progresses (Crialesi-Esposito et al., 2021; Mukherjee et al., 2019).

Another branch of numerical breakup investigations has focused on the morphology and behaviour of single drops placed in turbulent flows. Qian et al. (2006) published an early attempt to study the deformation and breakup of relatively small single bubbles (ρ_D/ρ_C < 0.1, μ_D/μ_C = 1, We = 0.6–5) injected into isotropic homogenous turbulence, concluding that breakup is preceded by a period of bubble oscillation. When breakup occurred, it was following a rapid and substantial deformation. Breakup was not, however, generally observed at the point of maximum deformation, but at a later time when some relaxation had already occurred.

Andersson and Helmi (2014) based their numerical breakup study on a large eddy simulation (LES) instead of a DNS. They concluded that breakup could be predicted from an energy barrier approach; with breakup taking place when the relative increase in surface energy exceeds a factor 1.4. Moreover, eddy visualization (Q-criterion) indicated that breakup takes place due to the interaction with a single eddy. This eddy was oriented perpendicular to the drop it deformed and this eddy was relatively large in comparison to the unreformed drop. These investigations were further refined in a later study by the same group (Karimi and Andersson, 2020), correcting the critical energy barrier to 1.5 after using a higher spatial resolution.

Shao et al. (2018) studied cascade breakup starting with a large drop of a low viscosity ratio emulsion (μ_D/μ_C = 1.0). Breakup was seen to follow a 'burst mode' where the drop was rapidly deformed in multiple directions before breaking into a large number of fragments. Shao et al. (2018) put special attention to the orientation of the drop interface and turbulent eddy (i.e., to high vorticity regions), concluding that the structures participating in the initial breakup of large drops tended to be tangential to the interface, whereas this alignment decreases as deformation and breakup progresses.

Komrakova (2019) studied breakup of single low-viscosity drops placed in homogenous and isotropic turbulence and identified different breakup mechanisms based on the initial drop-size. Relatively large drops (We = 30) break with a burst mechanism into a large number of fragments–similar to what was observed by Shao et al. (2018)–whereas smaller drops deform and break into fewer fragments. This could explain why burst mode breakup is typically not seen in experimental single drop breakup visualization studies, where the initial drops (i.e., We) is typically more on the lower range in Komrakova's study.

Recently, Rivière et al. (2021) studied the breakup of low viscosity- and density-ratio drops (i.e., gas bubbles) (μ_D/μ_D = 0.04), of sizes comparable to a few times the Kolmogorov-Hinze diameters (We = 3–45). These authors also show a pronounced difference in breakup morphology depending on how large the initial bubble is in relation to the Kolmogorov-Hinze scale. The smallest bubbles (We = 3) show a sequence of oscillations followed by subsequent breakup, primarily into two fragments. Somewhat larger bubbles (We = 6) show a similar initial breakup sequence but fragments (larger than the Kolmogorov-Hinze scale) continue breaking once more. Finally, large bubbles (We $\geq$ 15) break substantially faster and into a larger number of fragments. The authors discuss the results in terms of a difference in breakup time-scale. The breakup time of small bubbles is highly Weber number dependent and relatively long, whereas the breakup time of larger bubbles is short and relatively independent of Weber number.

Vela-Martín and Avila (2021) performed numerical experiments on a low viscosity ratio drop (μ_D/μ_D = 1, ρ_D/ρ_C = 1) breaking in homogenous isotropic turbulence, focusing on the correlation between drop deformation (stretching) and the vorticity ('eddies'), arguing that vorticity structures ('eddies') far from the drop interface (at a distance > 0.12 D, equivalent to > 6 η) dominate over inner eddies, i.e., vorticity structures close to the drop. At high We, the authors argue, both inner and outer eddies contribute to deforming the drop whereas at low We (We < ~3.5) the inner eddies are associated with drop relaxation, and thus counteract the deformation of the outer eddies. This goes against the popular assumption of breakup as caused by drop-eddy collisions.

Although representing substantial advances in their own right, it is far from obvious how to translate the insights gained from these previous numerical breakup studies to increase the understanding and efficiency of HPH emulsification in realistic applications. Most notably, these previous studies are typically performed with a substantially lower disperse phase viscosity, and it is well-known from applied emulsification investigations, that disperse phase viscosity contributes substantially to stabilizing the drop (Arai et al., 1977; Calabrese et al., 1986; Davies, 1985; Vankova et al., 2007), thereby influencing the deformation and breakup process.

The present contribution applies the numerical breakup experiment methodology to conditions closer to those in an industrially relevant emulsification device (i.e., a HPH used to process milk, or another high disperse phase viscosity product), than previous investigations. The aim is to improve the understanding of how turbulent interactions lead to breakup via deformations under conditions relevant to emulsification devices, with an emphasis on morphology of 'initial breakup' (Solsvik et al., 2016). This should be seen as the first step in such an attempt, and some simplifying assumptions are therefore necessary:.

(i) The turbulent field is approximated as being isotropic and homogenous. This assumption is based on the finding that local turbulent quantities behave fairly ideal in a HPH jet, at least for length-scales and positions relevant to drop breakup (Olad et al., 2021a, 2021b),
(ii) The investigations are limited to a relatively low Reynolds number, in order to limit computational cost.
(iii) The interfacial tension is assumed to be independent of time.

2. Ensuring conditions similar to the HPH

Predictions of the largest drop diameter surviving prolonged exposure to a turbulent field is traditionally based on the Kolmogorov-Hinze theory (Hinze, 1955; Kolmogorov, 1949), or one of the extensions thereof (Bałdyga and Podgorska, 1998; Calabrese et al., 1986; Shinnar, 1961; Tcholakova et al., 2011). Comprehensive comparisons of experimental emulsification data with proposed semi-empirical models suggest that the maximum drop diameter, after passing a low volume-fraction emulsion though an emulsification device, when operating in the turbulent inertial regime, can be predicted from (Arai et al., 1977; Calabrese et al., 1986; Davies, 1985; Vankova et al., 2007):.

$$D_{\max} = C_1\left(1 + C_2\frac{\mu_D\varepsilon^{1/3}D_{\max}^{1/3}}{\gamma}\right)\varepsilon^{-2/5}\gamma^{3/5}\rho_C^{-3/5} \quad (1)$$

with C_1 = 0.86 and C_2 = 0.37 (Vankova et al., 2007). Note that the original Kolmogorov-Hinze model (Hinze, 1955; Kolmogorov, 1949) is a special case of Eq. (1), obtained when the stabilizing effect of drop viscosity is assumed negligible.

Eq. (1) can be re-formulated in terms of the dimensionless numbers typically used to describe the conditions for numerical drop breakup investigations:.

$$We^{3/5} = C_1\left(1 + C_2\frac{\mu_D}{\mu_C}\left(\frac{\eta}{D}\right)^{4/3}We\right) \tag{2}$$

where the Weber number:

$$We = \frac{2\cdot\rho_C\cdot\varepsilon^{2/3}\cdot D^{5/3}}{\gamma} \tag{3}$$

denotes the ratio between disrupting turbulent inertial stress and stabilizing Laplace pressure and

$$\eta = \frac{\mu_C^{3/4}}{\rho_C^{3/4}\cdot\varepsilon^{1/4}} \tag{4}$$

denotes the Kolmogorov micro-scale. Note that the multiplying factor C_2 in Eq. (1) (which quantifies the stabilizing effect caused by drop viscosity), is re-expressed as a combination of viscosity ratio, drop diameter to Kolmogorov length-scale ratio and Weber number in Eq. (2). Thus, empirical emulsification experiments suggest that the breakup behaviour is controlled by three dimensionless numbers: We, η/D and μ_D/μ_C.

Turbulent flows are also characterized by a Reynolds number. Investigations of specific emulsification devices typically use a Reynolds number based on the average velocity and device geometry (Håkansson, 2019). Numerical breakup experiments are, however, most often performed in isotropic, homogenous turbulence with zero average flow, where it is more suitable to use a Reynolds number based on the scales of the turbulence, i.e., the Taylor-scale based Reynolds number (Pope 2000).

$$Re_\lambda = \frac{\rho_C\cdot u'\cdot\lambda}{\mu_C} \tag{5}$$

where u' is a RMS velocity and λ is the Taylor length-scale. Re_λ can be reformulated in terms of quantities that are more accessible in an applied setting, such as the (time-averaged) dissipation rate of turbulent kinetic energy, ε, and the integral length-scale of the turbulence, L (Pope, 2000):

$$Re_\lambda = \sqrt{\frac{20}{3}\frac{L^{4/3}\cdot\varepsilon^{1/3}}{\upsilon_C}} \tag{6}$$

A fifth dimensionless number, which is often suggested to have an influence on the breakup process in numerical studies is the density ratio, ρ_D/ρ_C. A sixth parameter to consider is the time the drops spend in the region of high turbulence in the emulsification device. In dimensionless form this can be expressed as the hold-up time divided by the Kolmogorov time-scale, T/τ_η, where.

$$\tau_\eta = \sqrt{\frac{\upsilon_C}{\varepsilon}} \tag{7}$$

Table 1 displays the value of these six dimensionless numbers for a HPH running milk at 25 MPa, operating at a homogenization temperature of 65 °C. The gap height (h) and average gap velocity (U_g) is calculated from the pressure loss correlation suggested by Phipps (1975) and the time-averaged dissipation rate of TKE is estimated from the scaling suggested by Mohr (1987) and Innings and Trägårdh (2007).

$$\varepsilon = \frac{U_g^3}{80h} \tag{8}$$

The hold-up time in the turbulent region of the HPH is approximated as the time required to travel a distance of 5 h at the gap velocity, U_g.

The disperse and continuous phase viscosities (milk fat and skim milk respectively) are obtained from Phipps (1985), the skim milk density is obtained from Kessler (2002) and the milk fat density is obtained from a general expression for fat (Singh, 2007).

Table 1 shows these scales for both a pilot scale and production scale HPH. As seen in the table, devices differ in turbulent conditions across these two industrially relevant scales. However, they are often found to perform similarly in terms of emulsification efficiency (Håkansson, 2016).

The drops entering an emulsification device under industrial conditions are polydisperse, implying that a range of both We and D/η are relevant for drop breakup in HPHs. Milk fat globules enter the HPH with diameters in the range 2–5 μm (Attaie and Richter, 2000), corresponding to We = 30–180 and D/η = 14–40. Milk fat globules exits with diameters in the range 0.5–1.5 μm (Di Marzo et al., 2016; Ransmark et al., 2019), corresponding to We = 2.9–23 and D/η = 3.7–11.

The numerical breakup experiments in the present study are setup with We = 1–60, covering the range from drops too small to break in the HPH to the larger drop entering the device. The density and viscosity ratios are set equal to those of milk fat (μ_D/μ_C = 22, ρ_D/ρ_C = 0.9). The length-scale ratio is set equal to 22, representative of an average of the values experienced in the HPH, see Table 1.

The time spent in the turbulent region differs by almost an order of magnitude between the pilot scale and production scale devices (T/τ_η = 20–100), a value in the upper region is chosen in the simulations (T/τ_η = 90), to capture all relevant breakup events. (No highly deformed surviving drops were found at simulation time T/τ_η = 90).

The Reynolds number is set to Re_λ = 33 in all simulations. It should be noted that this is lower than the values of a pilot or production scale HPH (see Table 1). This is a limitation of the current study, imposed to reduce computational cost. Decreasing the Re_λ corresponds to a narrowing of the inertial subrange, and as the inertial subrange narrows, the second similarity hypothesis becomes less applicable (Pope, 2000, p. 242). From a turbulent emulsification viewpoint, a lower Re_λ implies that the second order structure functions (appearing in the exact expression for the turbulent inertial stress assumed to break the drops) is over-predicted by the dissipation rate of TKE (Olad et al., 2021c; Solsvik and Jakobsen, 2016). Thus the Weber number, as defined by Eq. (3), over-predicts the ratio between disruptive inertial turbulent stress and stabilizing Laplace pressure. This should be kept in mind when interpreting the results. However, there are reasons to believe that the effect on the breakup morphology from the limited Reynolds number is still marginal (as long as the flow remains turbulent) since the empirical results do not suggest a Reynolds number dependence (Eq. (2)) when predicting the largest surviving drop diameter.

3. Methodology for numerical experiments

3.1. DNS and numerical method

The simulations are set up over a box with dimensionless length $L_{box} = 2\pi$ and periodic boundaries. An Arnold-Betrami-Childress (ABC) forcing (Mininni et al., 2006; Vallefuoco et al., 2017) is used to create an isotropic and homogenous turbulent flow inside the box. All three ABC amplitudes are set equal to 1.0. The dimensionless continuous phase viscosity is set to υ_C = 0.06 and energy is injected at the second wavenumber, to avoid the instability or artificial coalescence that can otherwise occur with the ABC forcing (Komrakova et al., 2015; Mukherjee et al., 2019; Podvigina and Pouquet, 1994).

Table 1
Relevant conditions and dimensionless numbers for drop breakup, comparing pilot and production scale HPH to the settings in the numerical experiments of this study.

		Production scale HPH	Pilot scale HPH	Numerical experiment (This study)
RELEVANT CONDITONS				
U_g [m/s]		214	103	–
h [μm]		138	11	–
ε [m^2/s^3]		$8.9{\cdot}10^8$	$13{\cdot}10^8$	–
DIMENSIONLESS NUMBERS				
ρ_D/ρ_C [-]		0.9	0.9	0.9
μ_D/μ_C [-]		22	22	22
Re_λ [-]		500	100	33
We [-]	D = 2–6 μm	29–180	38–240	1–60
	D = 0.5–1.5 μm	2.9–18	2.8–23	
D/η [-]	D = 2–6 μm	14–41	15–45	22
	D = 0.5–1.5 μm	3.4–10	3.7–11	
T/τ_η [-]		100	20	90

The Navier-Stokes equations are solved using an in-house DNS code where space and time discretizations are performed using second order accuracy central difference and Adams-Bashforth schemes, and an FFT solver is used for the Poisson equation. The interface between continuous phase fluid and the dispersed drop is described using the multi-dimensional tangent hyperbola interface capturing (MTHINC) algorithm (Ii et al., 2014; Rosti et al., 2019), a type of volume of fluid (VOF) method. The time step is adaptive and set to give a Courant–Friedrichs–Lewy number of 0.25.

More detailed description of the method, together with an overview of code structure and several validation cases, can be found elsewhere (Costa, 2018; Crialesi-Esposito et al., 2021; Rosti et al., 2019).

3.2. Interfacial area

Several methods have been suggested for calculating the interfacial area from a discretized VOF variable, α, but the most common approach is still to use the volume integral of the VOF gradient (cf. Guo et al., 2014; Soh et al., 2016),.

$$A(t) = \int |\nabla\alpha| dV \tag{9}$$

The rate of global interfacial deformation is quantified by the time derivative of $A(t)$, estimated with a five-point stencil scheme (fourth order method).

3.3. Vorticity visualizations

The Q-criterion (Hunt et al., 1988) is used below to visualize regions of high vorticity. A similar approach has been used in previous numerical breakup studies (Andersson and Helmi, 2014; Shao et al., 2018) to obtain first insights into the interaction between turbulent structures and the drop interface. However, it is important to interpret these visualizations with care. The Q-criterion will identify cores of these turbulent high-vorticity structures (often referred to as 'eddies'), but the number of such structures and their size will depend on the chosen cut-off. More elaborate methods for identifying turbulent structures have been proposed (Ghasempour et al., 2015; Haller, 2005) but are outside the scope of the current investigations.

3.4. Drop reconstruction

To ensure cost-efficiency in the simulations, the domain is modelled as a periodic cube (see Section 3.1). This creates a practical problem for identifying and visualizing breakup when drops cross one or more of the periodic boundaries. A reconstruction algorithm is therefore used for presenting the morphology results. Care was taken to ensure that this does not influence conclusions. Details of the algorithm and a comparison to raw isosurface visualization can be found in Appendix A.

3.5. Initialization and convergence

The flow variables are initialized by a zero field and run in one-phase mode until the average of the dissipation rate of TKE and Re_λ, across the entire domain, appeare to have converged (see Fig. 1). The convergence criterion is similar to the one used by Rivière et al. (2021). Both properties level out after approximately 400 τ_η. The one-phase flow is run for another 500 τ_η to collect averaged quantities (Re_λ = 32.9 and ε = 3.07, indicated by the dashed lines in Fig. 1). These time-averaged one-phase values are used in the definition of We, D/η and τ_η reported in connection to the settings and results.

To conduct a numerical breakup experiment, a spherical drop ($D_0/L_{box} = \pi^{-1}$, corresponding to a volume fraction of 1.7%) is injected into the one-phase flow and tracked over time, either until the first fragment detached itself or until time t = 90 τ_η (at which time the drop is considered to have exited the active region of the device). By varying the interfacial tension, a range of different We cases are investigated, see Table 2 (note that all length-scales in Table 2 are given in the primary dimensionless units used in the simulations). Drops of different We are injected on the same initial one-phase flow-field, allowing for a comparison of how drops of different We would behave if experiencing the same trajectory through the emulsification device. These simulations are marked as belonging to flow realization A in Table 2.

It is well known that the turbulent field varies stochastically, that instantaneous stresses can be considerably higher and lower than the time-average, and that these intermittent effects influence drop breakup (Bałdyga and Podgorska, 1998; Håkansson 2021; Kolmogorov, 1949). This implies that each drop passing the device experiences a different stress history. To account for this in the numerical experiments, three additional flow realizations are created (B-D in Table 2) by running the one-phase flow for an additional 100, 200 or 300 τ_η respectively, before injecting the drop.

3.6. Mesh resolution

A DNS is considered well resolved if the mesh size (Δx) is sufficiently small in comparison to the Kolmogorov length-scale. Eswaran and Pope (1988) suggests $\Delta x/\eta < 2\pi$, which implies that the current simulation ($\Delta x/\eta$ = 0.5) is well-resolved with respect

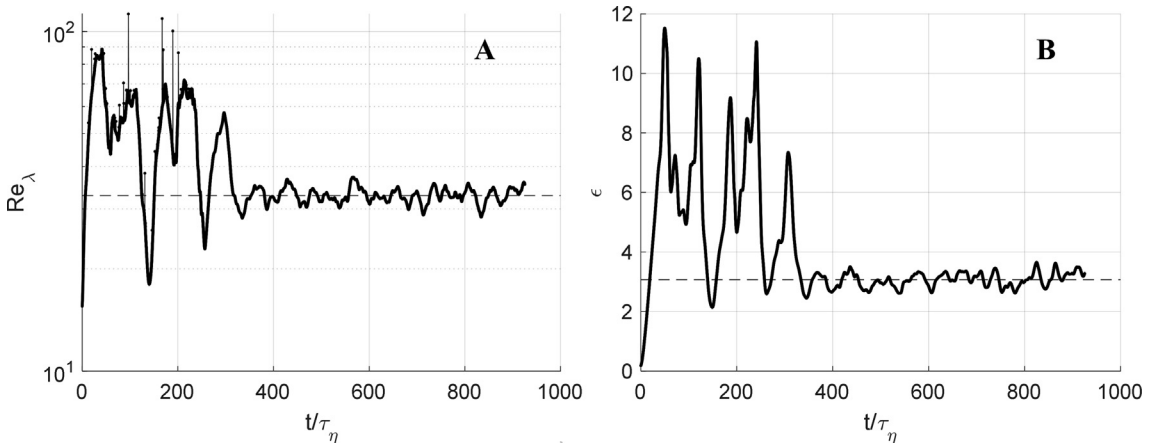

Fig. 1. Convergence prior to injection of the drop for (a) Re_λ and (b) ε, averaged across the computational domain.

Table 2
Simulated cases with primary settings (in the dimensionless units used in the simulation), calculated characteristic dimensions (also in the dimensionless form) with resulting breakup times (t_B/τ_η) and extents of global deformation (A/A_0) at point of initial breakup.

Flow realization	N [-]	D [-]	γ [-]	ν_C [-]	λ [-]	η [-]	We [-]	t_B/τ_η [-]	A/A_0at t_B
	PRIMARY SETTINGS				**CALCULATED**			**RESULTS**	
A	128	2	0.22	0.06	0.64	0.092	60	13.5	2.28
			0.45				30	13.2	2.11
			1.0				13	14.1	1.81
			2.7				5	21.44	1.74
			4.5				3	24.5	1.41
			13				1	NA	NA
B			0.45				30	23.8	2.34
			2.7				5	62.9	1.32
			4.5				3	73.6	1.32
			13				1	NA	NA
C			0.22				60	22.1	2.39
			0.45				30	34.6	2.71
			1.3				13	38.2	2.02
			2.7				5	50.0	1.39
			4.5				3	NA	NA
			13				1	NA	NA
D			0.45				30	19.45	1.60
			2.7				5	48.4	1.43
			4.5				3	54.9	1.33
			13				1	NA	NA

NA) No breakup detected before $t = 90\ \tau_\eta$.

to the flow of the continuous phase. However, the resolution across drop diameter ($D/\Delta x$) often becomes the limiting factor for breakup simulations. The setup in this study resulted in 41 grid points across the initial drop diameter. This $D_0/\Delta x$ is similar to that obtained in several similar numerical single drop breakup studies (Komrakova, 2019; Qian et al., 2006; Riviére et al., 2021), and it is also comparable to the initial drop diameter to pixel size typically obtained in experimental single drop breakup visualizations, see comparison in Håkansson (2020). Also note that the purpose of the study influences the required resolution; a higher resolution (measured in terms of $D_0/\Delta x$) is needed for studying the creation of small fragments or multi-stage breakup process than for studying the morphology at the initial breakup (as in this study).

To investigate the effect of mesh resolution on the results in this study, a test-case was set up where a drop was injected into a turbulent field (flow realization A) into three resolutions: (i) directly into the original flowfield (128^3, $D_0/\Delta x$ = 41), (ii) into the same flow-field to double resolution at (256^3, $D_0/\Delta x$ = 82) and (iii) into the flow-filed to half resolution (64^3, $D_0/\Delta x$ = 20). The turbulent forcing was turned off at the same time as the drop was injected (since the forcing operates on a fixed wave number), similar to what was done by Rivière et al. (2021), to test mesh sensitivity. The We based on the turbulence level before injection was set to 13 in these simulations, leading to a pronounced deformation (maximally so at t/τ_η = 17.9), followed by a relaxation (since forcing was turned off, the turbulence is decaying rapidly). The drop morphology at t/τ_η = 17.9 can be seen in Fig. 2 for the three different mesh resolutions. Morphological differences between the double resolution case (256^3, $D_0/\Delta x$ = 82) and the standard result case (128^3, $D_0/\Delta x$ = 41) are small, and the relative error in the interfacial area is<2 %. The half resolution case (64^3, $D_0/\Delta x$ = 20), still reproduces the general morphology but with a more staggered appearance, and with a relative error in surface area of 4.3 % (compared to double resolution). All further investigations are therefore conducted with $D_0/\Delta x$ = 41.

Another factor influenced by the mesh resolution is the risk of a gradual loss of mass, seen as a loss of the total disperse phase volume during the simulations. With the cases in Table 2, the relative loss of volume is below 0.022 %, comparing injection and initial breakup.

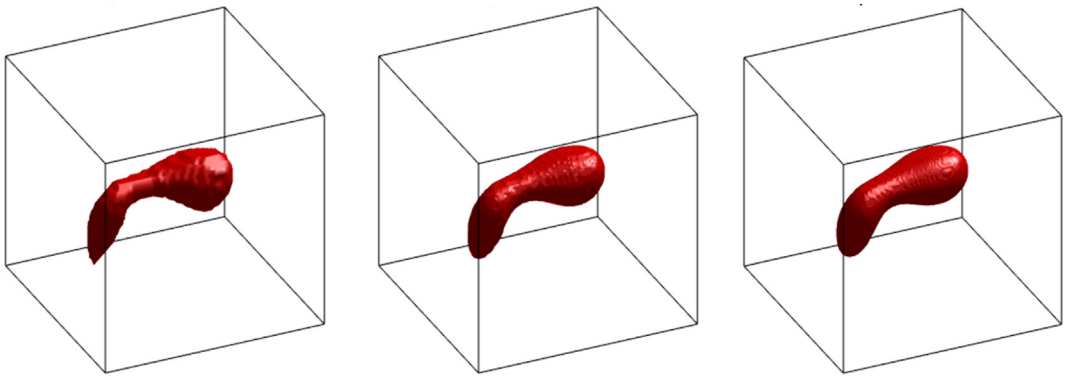

Fig. 2. Mesh resolution study, showing the drop morphology at t/τ_η = 18, for three mesh resolutions ($D_0/\Delta x$ = 20, 41, 82). (Decaying turbulence starting from We = 13 at t = 0).

4. Results and discussion

4.1. Drops at high Weber numbers ($13 \leq We \leq 60$)

As discussed in Section 2, the large drops breaking in an emulsification device have a We = 30 or higher.

4.1.1. Morphology at initial breakup

Fig. 3 displays how the drop morphology evolves over time for a drop with We = 30 (flow realization A). The drop starts deforming as soon as it is injected into the turbulent flow. It first elongates slightly into an approximately ellipsoidal shape (t/τ_η = 5.42), after which it is pulled into a sheet that starts bending (t/τ_η = 7.15). From t/τ_η = 8.64, we see how the sheet is pulled out in three different directions, forming three filaments/sheets, which have further deformed at t/τ_η = 10.7. At t/τ_η = 13.2, one of the necks has become sufficiently thin for the initial breakup to take place (green arrow). Continuing the simulations beyond this point, shows that the initial breakup event is followed by a rapid succession of continued breakup of the highly deformed large fragments.

As previously discussed, two drops injected in the flow at different times will show different deformation and breakup behaviour, due to intermittency effects in the turbulence. Fig. 4 shows the drop morphology prior to the detachment of the first fragment for all four flow realizations considered here (at We = 30). The time from injection to initial breakup differs between drops, however, severable similarities can also be seen among the cases in Fig. 4. First, note that initial breakup occurs relatively early (t_B = 13.2–34.6 τ_η, see Table 2) for all four cases. Also note the highly deformed structures in Fig. 4, where the drop has either been extended in multiple filament and/or sheets before breaking (A-C), or where large heavily deformed fragments are formed after the initial breakup (D). This behaviour appears to be consistent across a larger range of high Weber numbers, as seen in Fig. 5, showing the breakup morphology just prior to breakup for two of the flow realizations (A and C) at a lower (We = 13) and a higher We (We = 60); all these high-We cases show highly deformed structures, with multiple filaments extending in different directions. This behaviour has similarities to the burst-like breakup mechanism observed by previous investigators studying low viscosity systems (Komrakova, 2019; Shao et al., 2018). However, the higher viscosity in this study (μ_D/μ_C = 22 instead of 1.0) seem to promote longer and fewer filaments, as expected from the stabilizing influence of the viscous resistance to deformation and breakup.

For these high-We cases (We = 13–60), the deformation process is monotonic in the sense that the drop surface (and, hence, the interfacial energy) increases continuously until the initial breakup takes place, as seen in Fig. 6 showing the evolution of the interfacial area over time (upper panel) and its time derivative (lower panel). A positive derivative implies an increase in the total interfacial area, and thus a net increase in the interfacial energy (deformation), whereas a negative derivative indicates a net decrease in interfacial energy (relaxation). Note that the derivative remains positive throughout the process, showing that the drop never has a possibility to relax. This behaviour is consistent between the four flow realizations (Fig. 6). However, the extent of global deformation (as measured by the relative increase in interfacial area between the point of breakup and the initial spherical state), A/A_0, differ substantially between the cases (see Table 2); i.e., it is not possible to predict breakup simply as a consequence of reaching a critical increase in surface area, as is sometimes suggested in breakup frequency modelling (see review in Solsvik et al., 2013). The reason why the interfacial area is a poor predictor for when breakup takes place can be readily seen from the drop morphology at the point of breakup (Figs. 4-5); the initial breakup occurs when one of the filaments grows sufficiently thin (which is a local condition); this cannot be predicted using a global condition of net increase in interfacial energy (A/A_0), since the deformation morphology may substantially differ between drops even for similar values of A/A_0. The data in Figs. 4-5, suggest that the increase in interfacial area appears to be more related to the number of filaments than to the dimensions of the thinnest filament.

4.1.2. Turbulent structures and critical deformation

As discussed already in the methodology section, there are substantial challenges involved in any attempts to link drop deformation to specific localized turbulent structures. However, some additional insight into the breakup process might be obtained by comparing the drop morphology to high-vorticity flow structures. Fig. 7 displays the drop morphology (isosurface corresponding to the value of the VOF function α = 0.5) together with eddy visualizations (isosurface of Q = 30), focusing on the timespan where the drop is critically deforming. First, note that many turbulent structures can be seen in the vicinity of the breaking drop. However, some eddies appear to play a larger role than others. At t/τ_η = 4.1, the most prominent high vorticity structure, denoted (i)

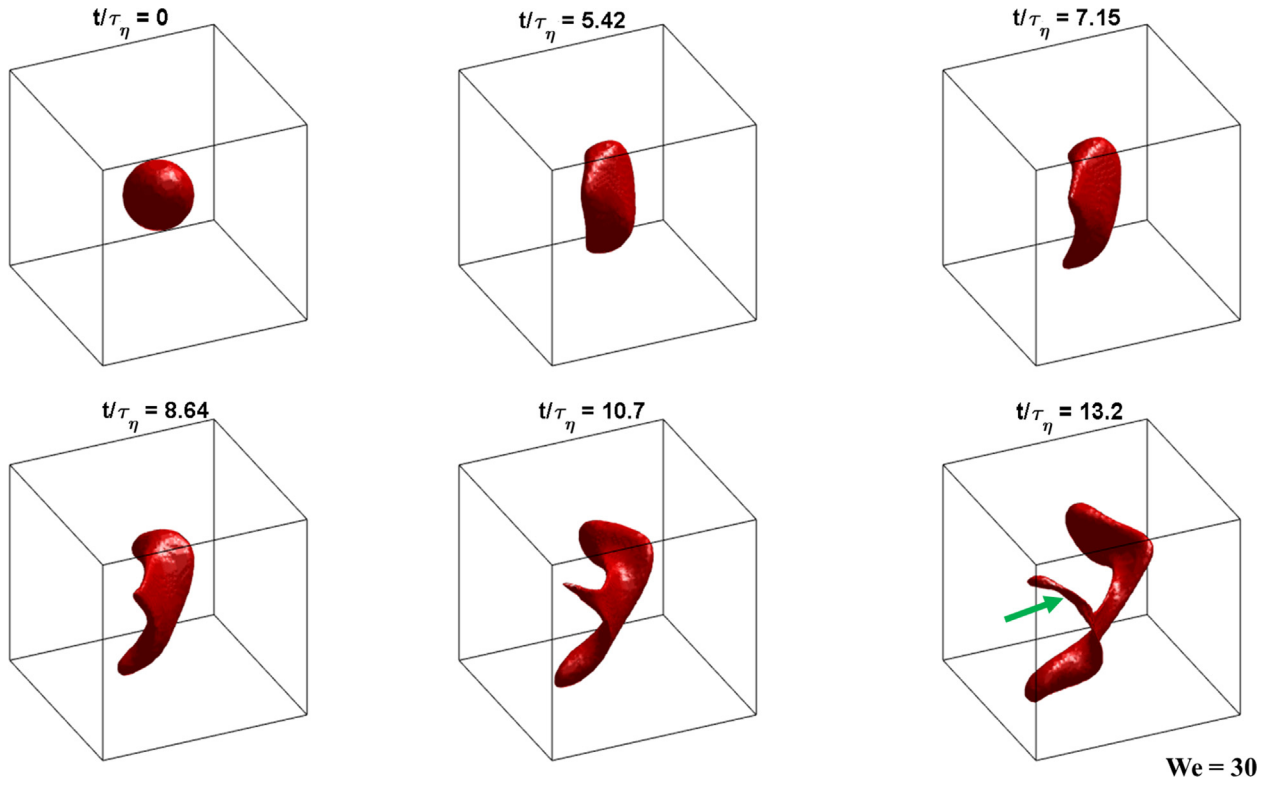

Fig. 3. Drop deformation sequence for We = 30 (flow realization A).

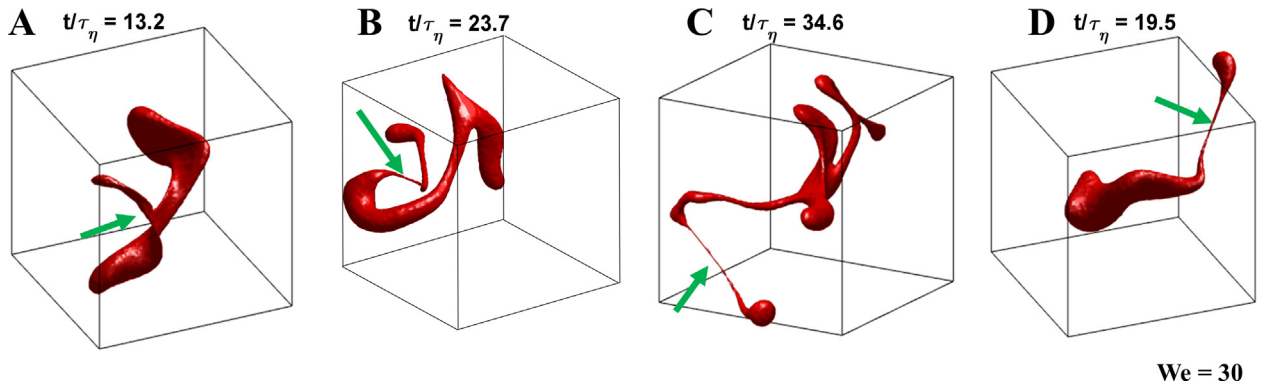

Fig. 4. Drop morphology at initial breakup We = 30 (flow realization A-D). The green arrows indicate the point of initial detachment.

in the figure, is aligned with the interface and appears to be involved in flattening the drop in the upper left part. This eddy-drop interaction is still apparent at t/τ_η = 5.4, but has almost completely dissipated before t/τ_η = 7.5. At t/τ_η = 4.1, we also see the emergence of another eddy, (ii), close to and aligned with the drop interface, pulling the flattened drop and deforming it into a bent sheet. This structure appears to loose energy fast due to its elongating action on the drop and has disappeared by t/τ_η = 7.5. Note that both these structures participating in the initial deformation are aligned with the drop, similarly to what was seen by Shao et al. (2018) for a low-viscosity system. A third interesting structure, denoted (iii), can also be seen already at t/τ_η = 4.1, in direct proximity to the upper right edge of the drop. As time progresses, this eddy gains in vorticity, pulls out a filament from the drop and twines itself around it (t/τ_η = 7.5–9.5), which leads to this filament growing further. This is also the filament where we observe the initial breakup to take place later, at t/τ_η = 13.2, see Fig. 3. Finally, we also see a fourth eddy, (iv), with high vorticity levels and a long life-time. However, this eddy remains at a distance from the drop during the entire process. The distance between the eddy core of (iv) and the drop might also help explain why it is more long-lived than for example eddy (ii): it does not appear to lose any energy in deforming the drop.

In summary, the eddy visualizations indicate that there is a collection of turbulent structures–varying in length- and time-scales–that interact with the drop. It is difficult to identify a single turbulent structure that dominates the process. This is also consistent with what was already deduced from the drop morphology in Figs. 3-5, showing the deformation of the drop into multiple filaments and sheets, a deformation pattern that is difficult to attribute to a single turbulent structure.

4.2. Drops at intermediate Weber numbers ($3 \leq We \leq 5$)

4.2.1. Morphology at initial breakup

Turning to the case of lower Weber numbers (comparable to the We of the smallest drops surviving passage through an emulsification device), we note that the breakup morphology is rather differ-

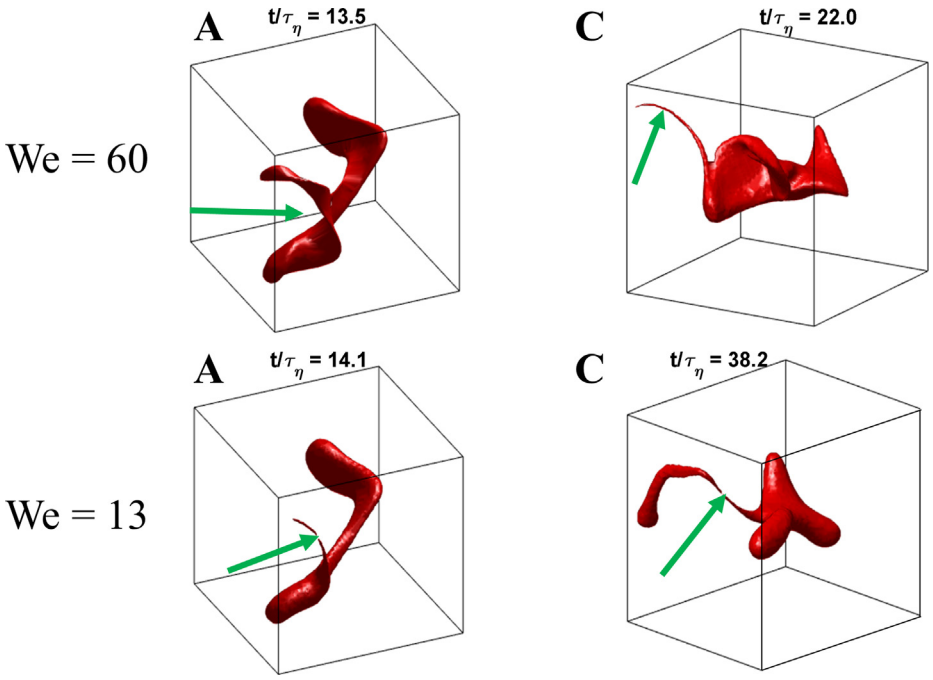

Fig. 5. Drop morphology at the first fragment detachment, showing two flow realizations (A and C) at two Weber numbers (We = 60 and 13). The green arrows indicate the point of initial detachment.

ent. In particular, Fig. 8 shows the drop morphology as a sequence of time-instances for We = 5. Already at t/τ_η = 3.59, the drop has started deforming into an ellipsoidal shape. It continues by elongating and flattening, mainly in one direction (t/τ_η = *7.16*). Keep in mind that this is the same flow realizations as in Fig. 3, and thus, at least initially, the same turbulent flow. Up to this point, the deformation is also similar to that seen at higher We. However, the low-We drop in Fig. 8 is pulled out in one direction only (t/τ_η = *10.7–14.2*) instead of flattening further as seen for the higher We case in Fig. 3. A neck growing into a long filament can be clearly seen at t/τ_η = 17.9, extended to a length of $\sim 3\ D_0$ at t/τ_η = 21.4, after which the drop is ready to break into two larger drops and a number of smaller satellites.

Fig. 9 (upper row) displays the drop morphology just before initial breakup, for all four flow realizations with We = 5. All four flow realizations lead to less complex deformation before breakup when compared to the high We cases; deformation primarily takes place in a single direction and eventually leads to the formation of a single filament that breaks when growing sufficiently thin. Moreover, flow realization A, C and D all show a distinct pattern of a filament forming between two larger drops that are approximately spherical, indicating that the breakup will eventually give rise to two larger daughters and an array of satellite drops. Conversely, the realization denoted as B displays the deformation to a smaller filament extending from a deformed structure containing most of the volume. In this case (B), the primary breakup will be closer to that of the high We cases, resulting in one or a few smaller drops together with a highly deformed larger drop (that is likely to break again if exposed to high turbulence intensity). The transition from a multidirectional 'burst-mechanism' to a unidirectional 'neck formation' mechanism is also similar to the observations made when comparing high to low We for a low-viscosity system in numerical breakup experiments (Komrakova, 2019), as to the transition from breakup into a larger number of fragments at higher We to a smaller number at lower We (Rivière et al., 2021). These observations can also be compared to drop breakup in high speed air jets where a transition between a 'vibrational mode' (oscillations followed by slow deformation) and a more violent, almost deterministic 'bag breakup' mode is often observed close to We = 13 (Kulkarni and Sojka, 2014; Soni et al., 2020).

The evolution of the surface area as a function of time can be seen in Fig. 10 (left panel), and displays notable differences between the different flow realizations. Whereas case A leads to a continuous deformation (much as for the high-We cases), cases B, C and D all display a sequence of deformations, followed by relaxation (regions of predominantly negative derivative) before reaching breakup. As expected from Figs. 9-10, the deformation at initial breakup is smaller than for the high-We cases (i.e., only one filament is formed for We = 5, leading to a less pronounced increase in the total interfacial area). Nevertheless, the global extent of deformation at breakup still varies substantially between flow realization (A/A_0 = 1.32–1.74, see Table 2).

It could also be noted that drops occasionally relax back to quasi-spherical conditions after having experienced a substantial degree of deformation. The drop of case D relaxes back again after reaching A/A_0 = 1.2. Moreover, case B reaches a global degree of deformation of A/A_0 = 1.33 at t/τ_η = 24.2, before relaxing back to A/A_0 < 1.1. It is noteworthy that the deformation at the time of initial breakup for flow realization B, is actually lower than the maximum deformation from which it was able to relax from. The reason is examined in Fig. 11, comparing the drop morphology at these two times. Although the global extent of deformation (A/A_0) is similar, the deformation at t/τ_η = 24.2 is in the form of a general elongation and flattening of the entire structure (a type of deformation that is possible to relax from) whereas at t/τ_η = 63.6, the same global extent of deformation is obtained in the form of a thin filament (which is difficult to relax back from). This finding does not necessarily imply that it is impossible to identify a global degree of deformation from which breakup is inevitable (i.e., a sufficient but not necessary criterion for breakup)–the deformation at t/τ_η = 24 is, after all, still lower than the critical level of 1.5 suggested by Karimi and Andersson (2019). However, this particular

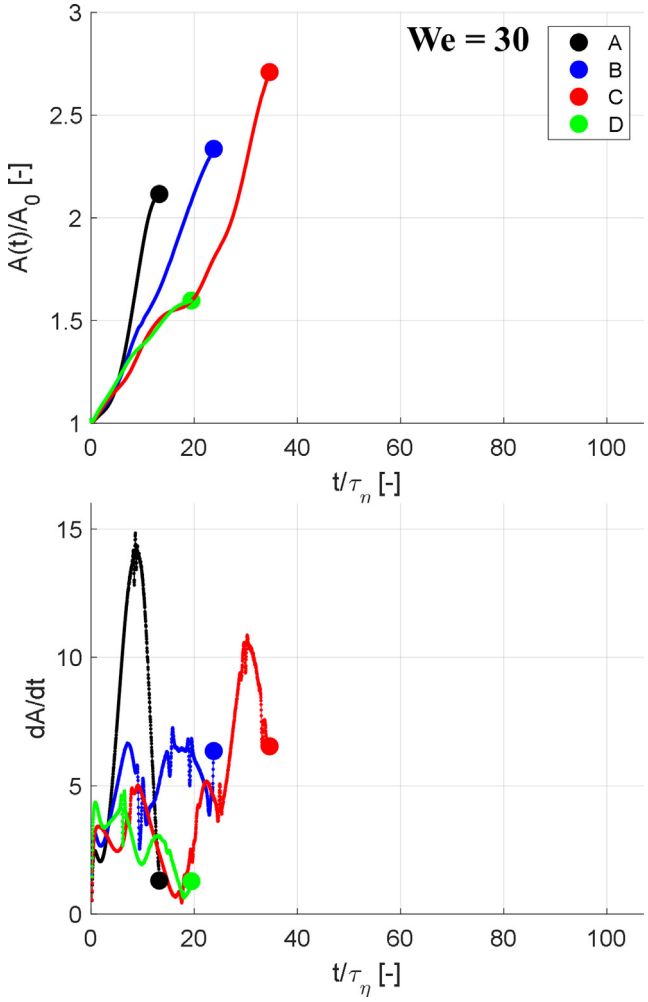

Fig. 6. Global deformation, $A(t)/A_0$ (upper panel) and rate of change of the global deformation (dA/dt) (lower pane), until the point of breakup (filled marker), for four flow realizations: A (black), B (blue), C (red) and D (green). (We = 30).

configuration does illustrate the challenges and pitfalls in using a global deformation measure as a tool for predicting breakup.

4.2.2. Turbulent structures and critical deformation

A plot showing the deforming drop and the turbulent eddies interacting with it is depicted in Fig. 12. Note that Fig. 12. and 7 are obtained with the same flow realization. Thus the turbulent eddies are expected to be similar (at least initially, before the interaction with the differently rigid drops will give rise to differences in the turbulence modulation). The same eddy structure discussed for the We = 30 case can be seen in Fig. 12, and appears to partake in the deformation. In particular, we see how eddy (i) initially has the same flattening effect on the drop (to a smaller extent, due to the higher resistance to deformation). Moreover, the aligned and short-lived eddy (ii) appears to play a role in elongating the drop between t/τ_η = 3.6 and t/τ_η = 11.0. The eddy that appeared to drive the pulling out of the thin filament that was the first to break at We = 30 (eddy iii), is still present but is now unable to pull out a filament from the more energetic surface. At t/τ_η = 11.0 it is still present but the drop is moving away from it. Instead of winding on the filament, eddy (iii) aligns with the drop and appears to contribute to elongating it together with (ii). Since breakup occurs later at We = 5 than at We = 30, new turbulent structures also come into play. At t/τ_η = 8.0 (when eddy (ii) is decreasing in vorticity level) we see another aligned high-vorticity structure, denoted as (v), contributing to drop elongation. This structure appears to continue elongating the drop at t/τ_η = 11 into the direction of which the thin filament responsible for initial breakup will eventually form.

In summary, although we see a different breakup morphology, it is still difficult to identify a single turbulent structure as responsible for causing critical deformation or breakup. The challenges with using this type of visualizations to draw conclusions about the number of interactions are many, however both eddies (ii) and (v) appear to contribute to the critical elongation, and they behave differently, suggesting that they are separate turbulent structures.

4.2.3. Comparing between We in the intermediary range ($3 \leq We \leq 5$)

The morphology visualizations at initial breakup in Fig. 9 also show the results at a somewhat lower We (We = 3), and illustrate how the behaviour is similar but with an even more pronounced deformation into two approximately spherical sub-drops separated by a thinning filament. Also note that breakup occurs consistently later (or not at all within the investigated time-span, see case C) when decreasing We from 5 to 3. Both of these observations are consistent with the fact that a more rigid interface gives more time for the dispersed phase volume to relax into a spherical shape if the critical filament has not formed. Moreover, in the case of breakup, stiffer drops form two larger daughter drops and a collection of smaller satellites.

Fig. 10 displays how the drop interfacial area evolves over time for We = 3 and the four different flow realizations. For flow realization A, the drop deforms monotonic and breaks (as in the previous cases), whereas for B and D, the drop goes through a number of deformation-relaxation cycles before finally deforming critically and breaking. Flow realization C also displays oscillations, with the last deformation reaching a value of the global deformation A/A_0 = 1.2; nevertheless, the drop, relaxes again and no breakup occurs before the simulation end-time (t/τ_η = 90). The We = 3 simulations illustrate how the stochastic variations in the turbulent field are linked to the drop survival probability, and how a critical Weber number is a stochastic property when seen on the level of individual drops. Drops entering at flow conditions A (which is, apparently, at a point in time with exceptionally high instantaneous stress at the position where the drop is injected) will break fast even if they are very small or poorly stabilized (i.e., having a relatively low We), whereas drops entering the flow at flow conditions C (a point in time with lower stresses at the centre of the domain is less intense), will survive beyond t/τ_η = 90 for $We \leq 3$.

The breakup morphology observed for these drops in the intermediate We range ($3 \leq We \leq 5$) are comparable to the conditions in experimental studies, allowing for a qualitative comparison. The formation of a large number of satellites (the number of which is growing with increasing We) has also been reported in experimental studies (Ashar et al., 2018; Herø et al., 2020). These results of the numerical breakup experiments are also in line with the observations based on the emulsification experiments by Tcholakova et al. (2007). Using an inverse population balance equation method, Tcholakova et al. (2007) retrieved the daughter drop probability distribution function and concluded that for highly viscous drops (as those considered in this study), breakup generates two approximately equally sized fragments separated by a long filament, subsequently breaking into several smaller droplets.

4.3. Drops at low Weber numbers (We = 1)

None of the simulations at We = 1 resulted in a breakup events before t/τ_η = 90 (time chosen to correspond approximately to the time at which drops would leave the efficient region of breakup in the HPH). To analyse these flow cases, Fig. 13 displays the drop morphology through a sequence of images for flow realization A, with the global deformation (A/A_0) reported in Fig. 14, for all four

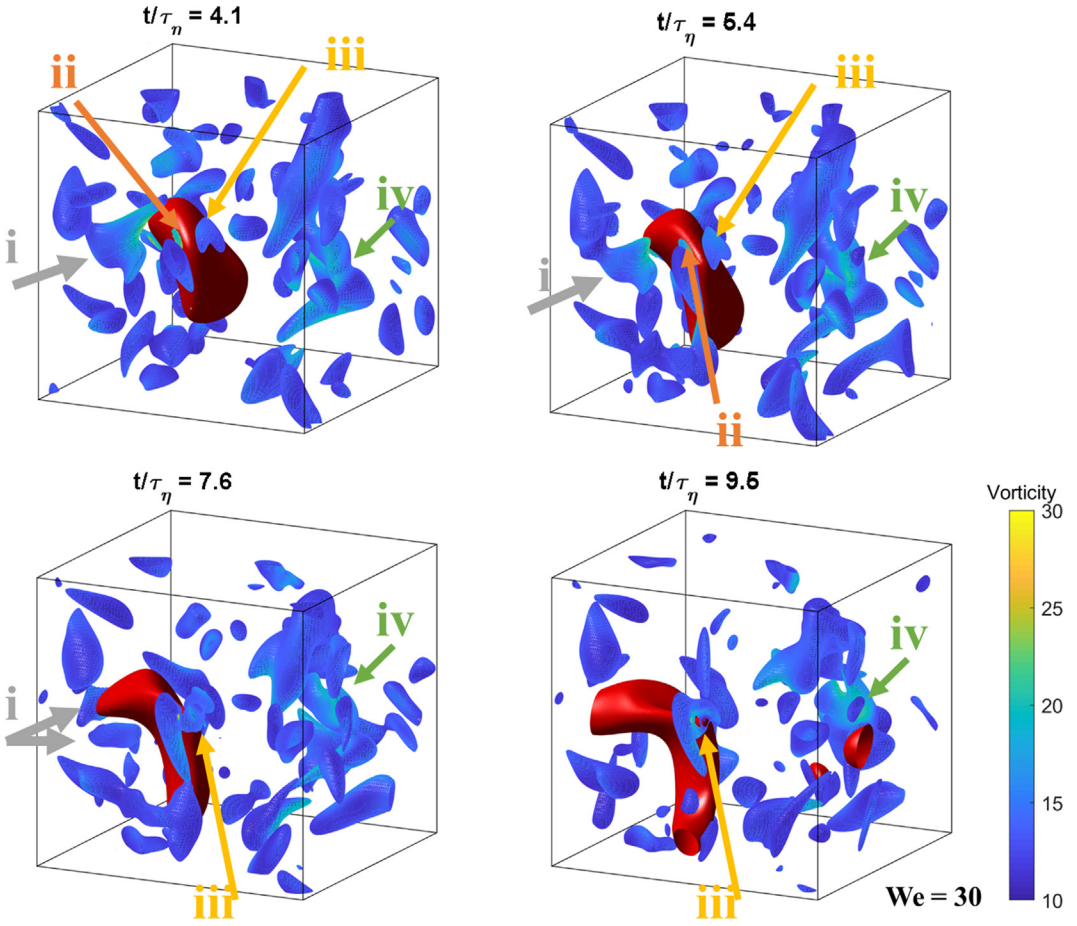

Fig. 7. Simultaneous visualizations of deforming drops (red isosurfaces) and Q-criterion turbulent structures (vorticity coloured isosurfaces) for the configuration We = 30 and flow realization A.

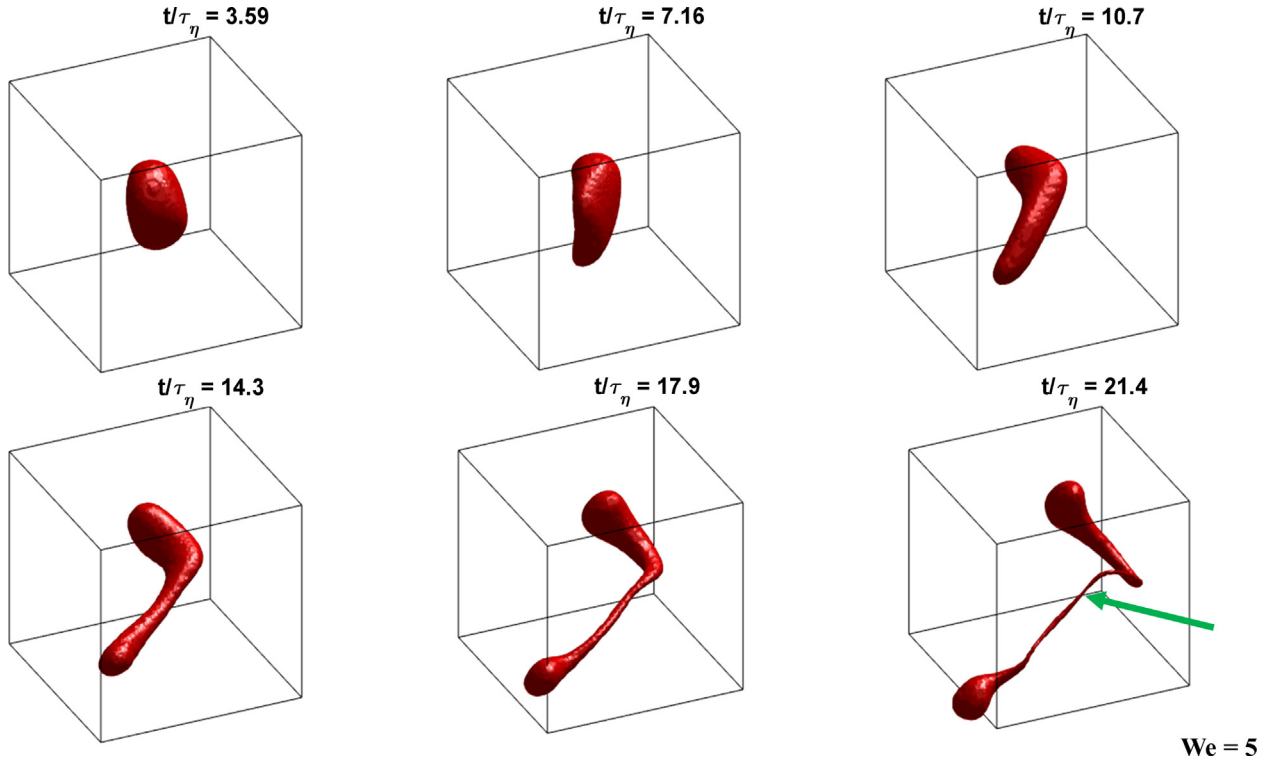

Fig. 8. Drop deformation sequence for a flow configuration at We = 5 (flow realization A).

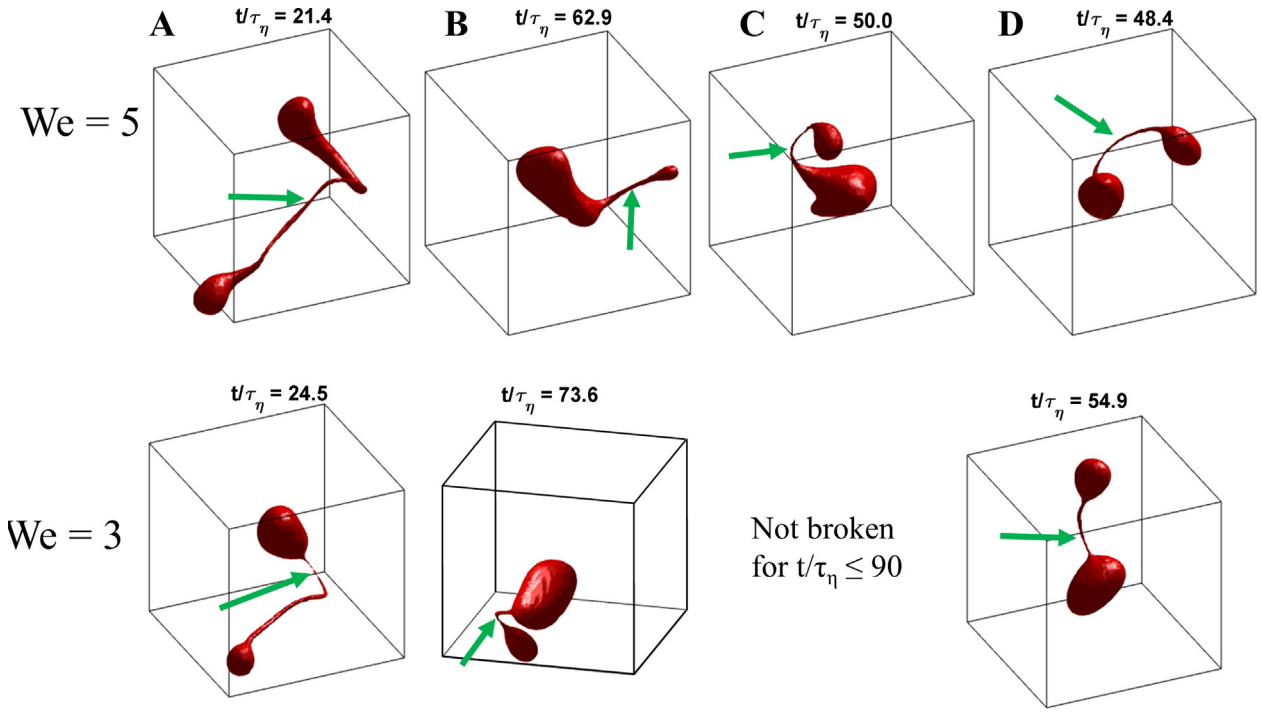

Fig. 9. Drop morphology at initial breakup for cases with We = 3 and 5 (flow realizations A-D). The green arrows indicate the point of initial detachment.

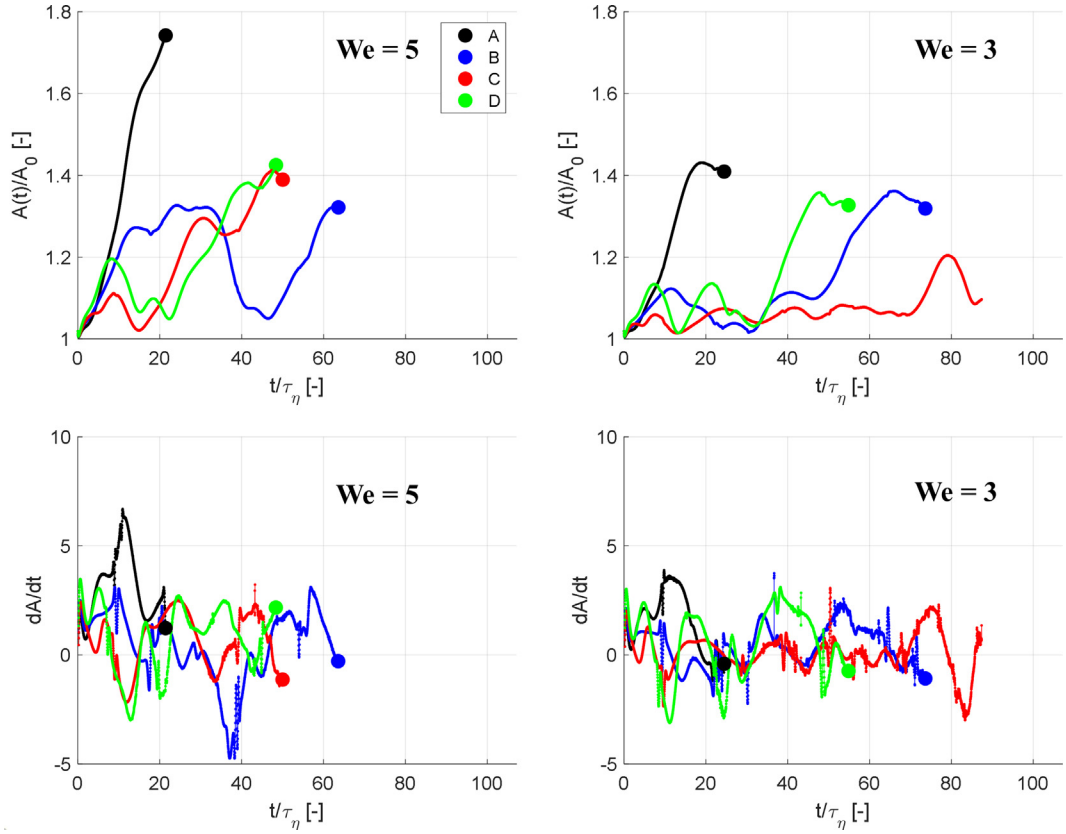

Fig. 10. Global deformation, $A(t)/A_0$ (upper pane) and rate of change of the global deformation (dA/dt) (lower pane), until the point of breakup (filled marker) for four flow realizations: A (black), B (blue), C (red) and D (green). Left size: We = 5. Right side: We = 3.

flow realizations. As seen in the figures, the drop goes through a periodic deformation and relaxation. None of the deformations are, however, effective enough to pull out a filament or lead to the formation of a neck (see Fig. 13), which explains why no breakup is eventually observed. It could be noted that there is a tendency for an increased deformation amplitude over time in

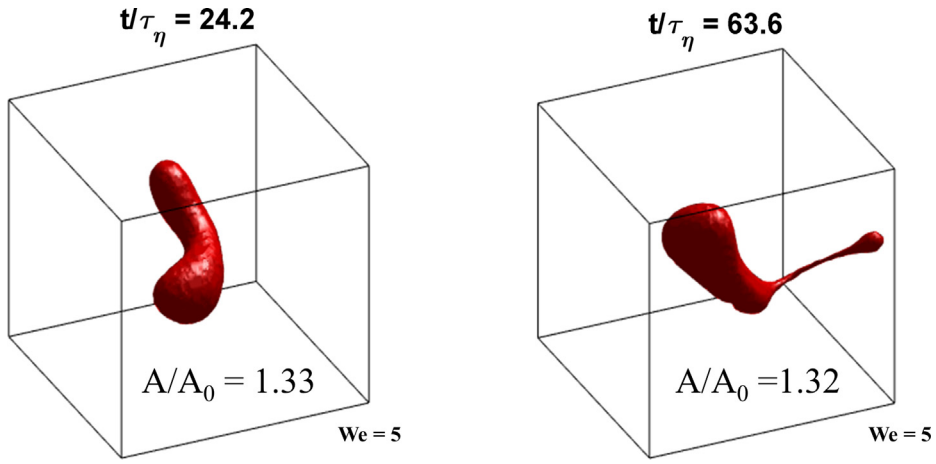

Fig. 11. Comparing a deformed state the drop relaxes from (left) and a deformed state the drop does not relax from (right), corresponding to approximately the same global deformation, A/A_0 = 1.3 (We = 5, flow realization B).

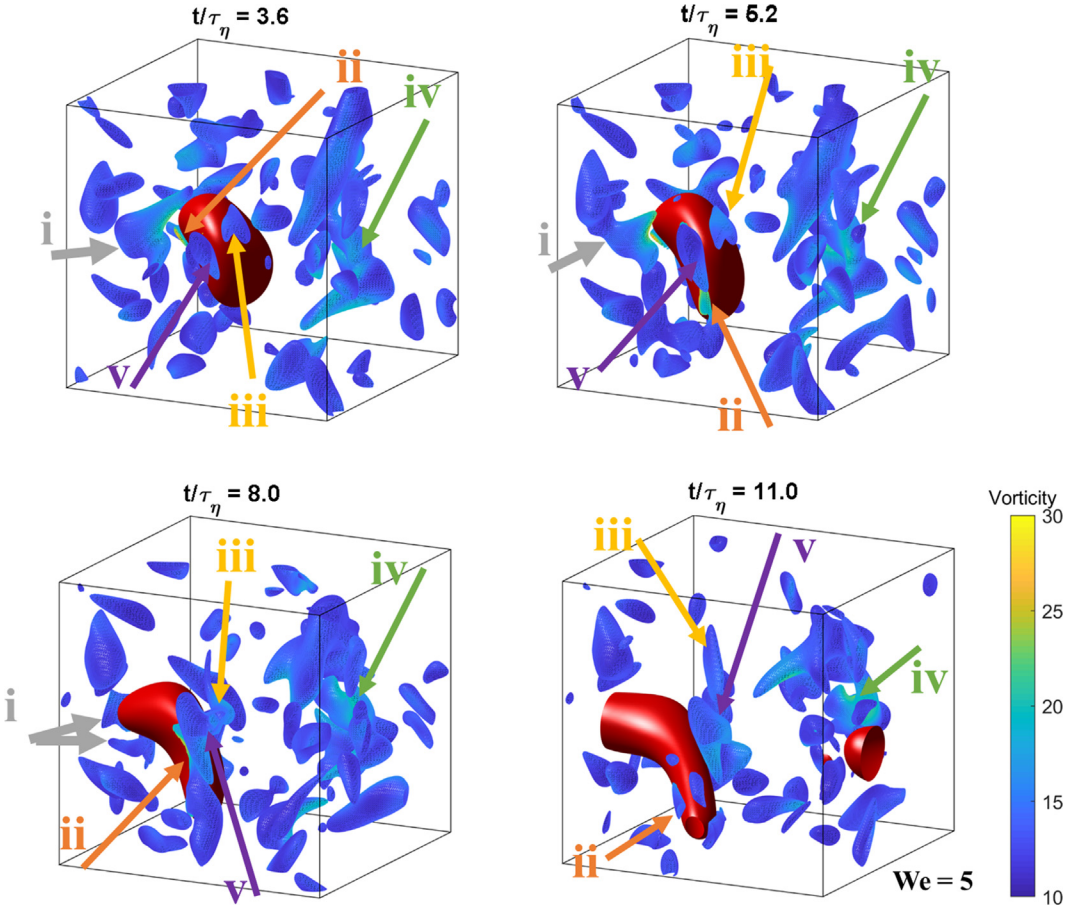

Fig. 12. Simultaneous visualizations of deforming drops (red isosurfaces) and Q-criterion turbulent structures (vorticity coloured isosurfaces) for the configuration We = 5 and flow realization A.

Fig. 14, but that the global extent of deformation is still exceedingly low (A/A_0 < 1.06) as compared to the levels where breakup is observed at higher We, see Figs. 6 and 10.

4.4. A two-stage process: Oscillations and critical deformation

Looking at the results in Sections 4.1-4.3, it is reasonable to describe the interaction between the drop and the continuous phase–from injection to initial breakup–as a two-step process: an oscillatory phase and a critical breakup phase. Similar interpretations can also be deduced from drop breakup experiments (Herø et al., 2020). The oscillatory phase consists of a sequence of deformation and relaxations where the global deformation can become exceedingly large ($A/A_0 \sim 1.3$ is observed) but without the formation of the necks or filament that lead to breakup. The critical breakup phase can be identified as when the drop goes into a

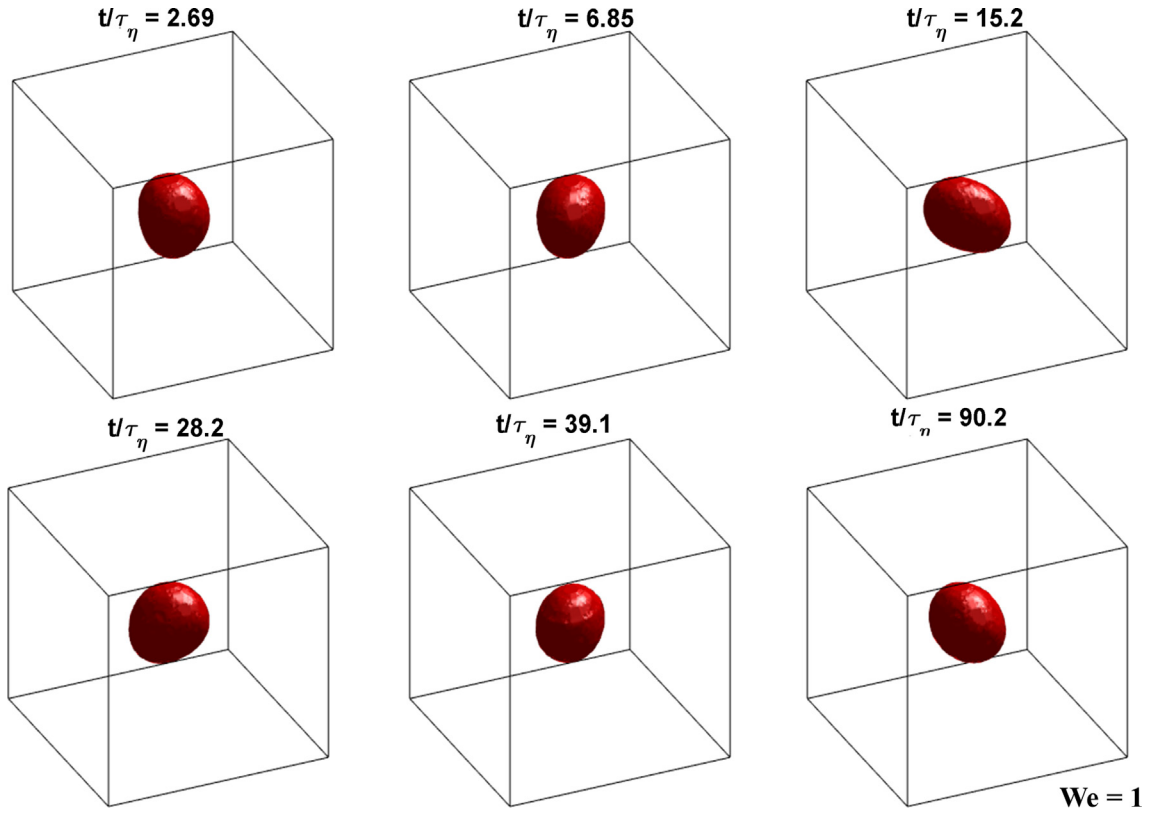

Fig. 13. Drop deformation sequence for a configuration with We = 1 (flow realization A).

monotonic deformation sequence (e.g., starting at t/τ_η = 46 for flow realization B, We = 5, and at t/τ_η = 23 for flow realization D, We = 3). As noted previously, the global deformation in the breakup phase is not necessarily larger than in the oscillatory phase (as seen for flow realization B in We = 5, Fig. 11), but it leads to the formation of instable structures that once formed will deterministically break. Drops with low We are less likely to enter the breakup phase (at least when holdup time in the turbulent zone is limited), whereas drops with a high We have a higher probability of going directly into the breakup phase without passing though the oscillatory phase. It is, however, not possible to make any quantitative statements about these probabilities and their dependence on We at this point (since this would require studying a substantially larger number of flow realizations).

The observation of an oscillatory phase may lead to the identification of three cases, based on the value of the Weber number We: a high We regime with direct breakup, an intermediate We regime leading to oscillation followed by likely breakup, and a low We regime corresponding to oscillations without breakup. These distinctions are similar to what has been observed for low viscosity drops in experimental single drop breakup visualizations (Risso and Fabre, 1998). For the low viscosity system, it has been showed that this behaviour also arises when modelling the drop-fluid interaction with a Rayleigh-Lamb model, describing the drop interface as a linear oscillator that deforms ('stretches') and relaxes with a characteristic frequency f_2 and with a dampening rate β_2 (Risso and Fabre, 1998). The resulting Rayleigh-Lamb model has also proven highly fruitful in predicting breakup in subsequent studies (Galinat et al., 2007; Lalanne et al., 2019). Some aspects of this model are in agreement with the high viscosity-ratio simulation results of the present study. Specifically, a characteristic property of such a Rayleigh-Lamb model is that it predicts an oscillation amplitude that grows over time, as a consequence of a resonance phenomenon (cf. Fig. 14). Moreover, for the configurations considered in this study, the theoretically predicted oscillation period is $1/f_2$ = 32–5.5 τ_η, with the highest value obtained for We = 30 and the lowest value for We = 1 (calculated using the algorithm suggested by Miller and Scriven, 1968). This corresponds roughly to the simulation results in the present study, which displays an oscillation period of $\sim$ 10 τ_η *for We = 1–5* (see Figs. 10 and 14). However, there are also discrepancies between the Rayleigh-Lamb model and the results in the present study. Due to the high viscosity of the disperse phase in the present study, the dampening frequency, β_2, becomes exceedingly large: The dampening in the Rayleigh-Lamb model is often described in dimensionless form as (Lalanne et al., 2019; Risso and Fabre, 2019):.

$$\xi = \frac{\beta_2}{2\pi \cdot f_2} \tag{10}$$

Using the full implicit formula (Miller and Scriven, 1968) to calculate the characteristic frequency f_2, and dampening rate β_2 for the cases in Table 2, results in values in the range ξ = 0.6–5 (lowest value for We = 1). Indeed, following the results in Lalanne et al. (2019), possibilities for such a resonance mechanism seems to be limited already for ξ > 0.3. This suggests fundamental differences between mechanisms driving oscillations between low and high viscosity ratio systems.

Turning to the time required for the drop to break under these conditions, Fig. 15 (left panel) displays the time between injection and the initial breakup (t_B). The figure illustrates the same behaviour as discussed above; time from injection to breakup varies between flow realizations (for the same We) but more so at lower We. Moreover, the average time decreases with increasing We. The empirical lifetime correlation suggested by Rivière et al. (2021) for drops of low viscosity (μ_D/μ_C = 0.04).

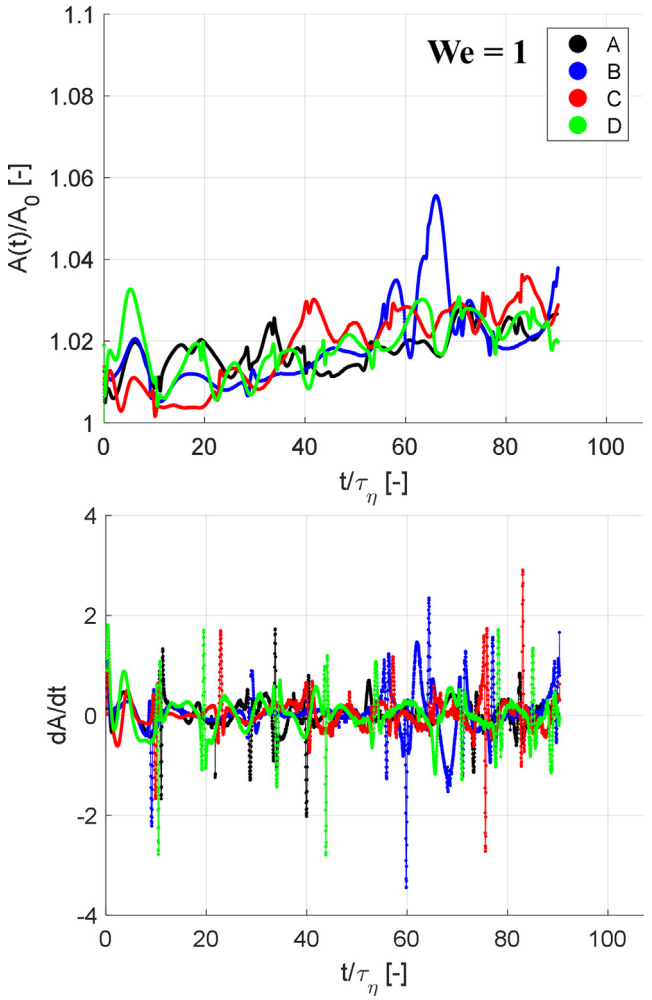

Fig. 14. Global deformation, A(t)/A_0 (upper panel) and rate of change of global deformation (dA/dt) (lower panel) for four flow realizations: A (black), B (blue), C (red) and D (green). We = 1.

$$t_B = \frac{2}{3} \cdot D_0^{2/3} \cdot \varepsilon^{-1/3} \frac{1}{\sqrt{We/3 - 1}} \tag{11}$$

is displayed in the figure with a black solid line. As seen in the figure, the drop lifetime is substantially higher at higher viscosities (this study). However, the same scaling is able to reasonably well describes the observed We-dependence properly rescaled, as seen from the dashed blue line. This reports the correlation in Eq. (11) with the proportionality constant adjusted to a value of 112 to better fit the high-viscosity data of our simulations.

As discussed above, the process from injection to initial breakup can be divided into two phases; note that t_B in Fig. 15 (left panel) is the time for the entire process. Part of this time is spent in deformation-relaxation cycles, with drops which are in several cases in a relatively relaxed state when entering the deformation phase (see Fig. 10). Thus, the We-dependence of the breakup time is not necessarily a consequence of the different amount of time required to critically deform the drop (Zhou et al., 2021), but it is also a measure of how long time a drop spends in the oscillatory phase.

The right panel of Fig. 15 displays the time spent in the final deformation phase, t_B^* (from start of monotonic deformation, $dA/dt > 0$, until first detachment) for all drops observed to break in the present study. Note that typically $t_B^* = t_B$, for the high We cases, and $t_B^* < t_B$ for lower values of We. As seen in the figure, the We-dependence disappears when correcting for the oscillatory phase ($t_B^*/\tau_\eta = 23.5 \pm 7.8$), suggesting that, once experiencing conditions intense enough to critically deform the drop, the deformation time is independent of We.

4.5. Current limitations and suggestions for continued investigations

The long-term aim of these investigations is to increase our understanding of drop breakup and emulsification in industrially relevant emulsification devices, such as the HPH, for drops where the disperse to continuous phase viscosity ratio is large (as is the case in the majority of applications).

As stated in the introduction, the current study has simplifying assumptions, relaxing these provides opportunities for new investigations and improved understanding. The use of isotropic homogenous turbulence (instead of the flow in the actual device) is one such limitation. Even if the small scale turbulent scales responsible for breakup is similar (as suggested by recent DNS investigations, Olad et al., 2021a, 2021b, 2021c), the turbulence in an emulsification device is highly inhomogeneous, leading to a larger variation of the time-history of instantaneous stresses in the industrially relevant device. Extending the current investigations to a DNS on the actual device would constitute an interesting continuation.

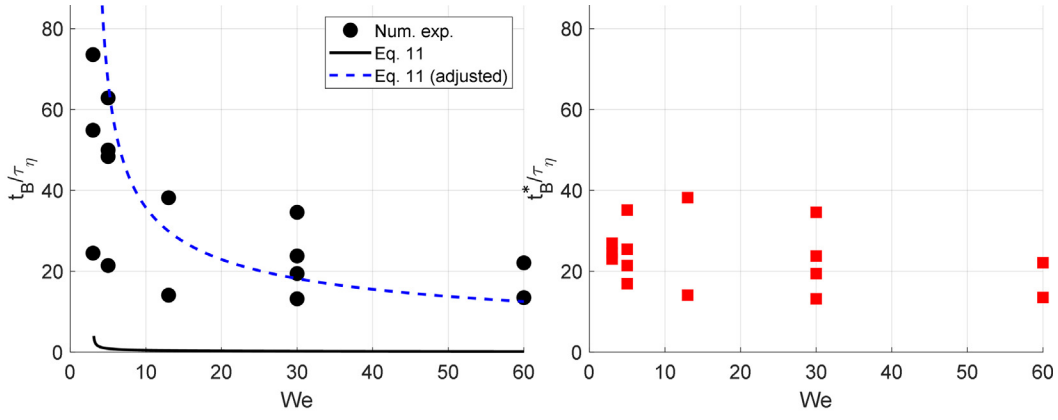

Fig. 15. Time from injection to initial breakup (t_B) as a function of We (left pane), and time in the breakup phase (t_B^*) as a function of We (right panel). The solid black line shows the empirical lifetime correlation suggested by Rivière et al. (2021), Eq. (11) in the text. The dashed blue line indicates the same correlation with the proportionality constant adjusted to fit the high-viscosity data (see text).

Another limitation is the relatively low Reynolds number (a common limitation in this type of investigations, due to the computational cost of interface-resolved simulations). As discussed in Section 2, Reynolds number does not enter the empirical dimensionless number correlation (Eq. (2)), but a Reynolds number below 100 leads to a change in the behaviour of the second-order structure functions, and thus indirectly influences the turbulent stresses and their dependence on the turbulent length-scale. Thus, extending these investigations to higher Reynolds numbers would be interesting for future studies.

A third assumption is that the interfacial tension is assumed to be constant over time and space, whereas the dynamic adsorption of surface active molecules and particles will influence the interfacial tension (and make it non-uniform). These time- and spatial-variations in interfacial tension are expected to have an effect on the breakup morphology. Models for tracking the dynamics of surfactants and interfacial tension have been suggested in different frameworks (Alopaeus, 2022; Håkansson et al., 2009; Skartlien et al., 2013), and including this in a numerical breakup model is possible. However, substantial work still remains to be done on how to describe this, especially for the more industrially relevant case of high-molecular emulsifiers (e.g., proteins, and protein aggregates).

Finally, it can be noted that further comparisons between numerical '*in silico*' experiments and single drop '*in vitro*' high-speed breakup visualization experiments on the same system would also be of interest for further studies. As discussed in Section 1, both methodologies have their advantages and limitations, suggesting that combined investigations could be of great value.

5. Conclusions

The present numerical single drop breakup experiments, on drops with a high disperse to continuous phase viscosity ratio, suggest that the breakup morphology is highly dependent on the Weber number. In a practical application, a range of drop sizes enter the device. High We drops (the largest drops entering the device), tend to deform in multiple directions simultaneously. Initial breakup occurs when one of the many filaments or sheets becomes sufficiently thin. Intermediary We drops (the smaller drops entering the device) deform in a single direction, with the formation of a thin filament separating two almost spherical sub-drops. This leads to the formation of two approximately equally large fragments and an array of smaller satellite drops after the primary breakup. Attempts to correlate the deformation with the evolution of eddy structures are difficult but indicate that more than one turbulent eddy is involved in the process of causing the final critical droplet deformation.

The process from injection of a drop until initial breakup, can be divided into an oscillatory phase (cycles of increasing and decreasing interfacial area) and a final breakup phase (a monotonic increase in the degree of deformation until critical deformation), as also observed in experimental studies as well as in numerical studies on low viscosity systems. The larger the We (i.e., the larger the drop), the higher is the probability to pass straight into the breakup phase. The lower the We, the less likely it is to reach the breakup phase (within a finite time-period). Again this is in agreement with what has been observed for low viscosity-ratio systems, but cannot be explained by the same mechanism due to the substantially higher dampening rates obtained at high drop viscosities.

We also show that the initial breakup time, as measured from when the drop enters the turbulence until the first fragment is detached, decreases with We, with a We-dependence similar to what has been reported in previous studies on low-viscosity systems. However, the time required for the drop to finally break, after a varying number of oscillations, is relatively independent of the Weber number ($t_B^*/\tau_\eta \sim 24$).

CRediT authorship contribution statement

Andreas Håkansson: Conceptualization, Formal analysis, Writing – original draft, Funding acquisition. **Luca Brandt:** Methodology, Software, Resources, Writing – review & editing.

Declaration of Competing Interest

The authors declare that they have no known competing financial interests or personal relationships that could have appeared to influence the work reported in this paper.

Acknowledgements

Dr Marco Crialesi Esposito is gratefully acknowledged for customizing, supplying and supporting AH on using the DNS code, as well as for valuable discussion on turbulence-drop interactions. Prof. Fredrik Innings and Peyman Olad are gratefully acknowledged for valuable discussions on the nature of turbulent drop breakup and homogenization. This research was funded by The Swedish Research Council (VR), grant number 2018–03820, and Tetra Pak Processing Systems AB.

Appendix. A. Effect of drop reconstruction

The numerical single drop breakup visualizations were carried out in a periodic box domain. This allows efficient use of computational resources. However, every time a drop, or a filament thereof, crosses over one of the six boundaries, it will appear truncated in a raw VOF-isosurface plot. The left column of Fig. A.1 shows these raw isosurfaces for two of the cases discussed in the results section. From a pedagogic or reader-oriented perspective, this is problematic since it is easy to misinterpret such a figure from a hasty view (i.e., the drop drops in the left column of Fig. A.1 appears to already have been fragmented). It becomes increasingly difficult to correctly interpret drop morphology for cases with more complex deformation (see lower panel in Fig. A.1).

The current study uses a reconstruction algorithm to translate the isosurfaces (left column in Fig. A.1) into reconstructed drops (right column of Fig. A.1). The reconstruction proceeds with the following steps:.

1) The grid points with $\alpha > 0.5$ are stored in a matrix P.
2) P is mirrored in each of the six periodic planes, and stored into a new matrix R.
3) An alpha shape (a generalized convex hull) algorithm (Edelsbrunner et al., 1983) (used as implemented in MATLAB 2019a, with a cut-off radius of 0.1) is used to identify all bounding volumes. Due to the mirroring, the whole drop will appear at least once.
4) The largest alpha shape-objects (i.e., one of the representations of the whole drop) is selected and displayed.
5) A box with the same size as the original computational domain is plotted as an overlay, for scale references, centred at the drop volume centre. (Note that the mirroring leads to that the reconstructed drop can be longer than the length of the box and, thus, is not always fully contained within this original box.)

The right column in Fig. A.1 displays the resulting reconstructed drops. As seen, the reconstruction does not alter the morphology, but results in a substantially clearer view of it. It should also be noted that the reconstruction does lead to the drop surface appearing slightly less smooth (compare the surface structure between columns in Fig. A.1). However, no further post-processing was used

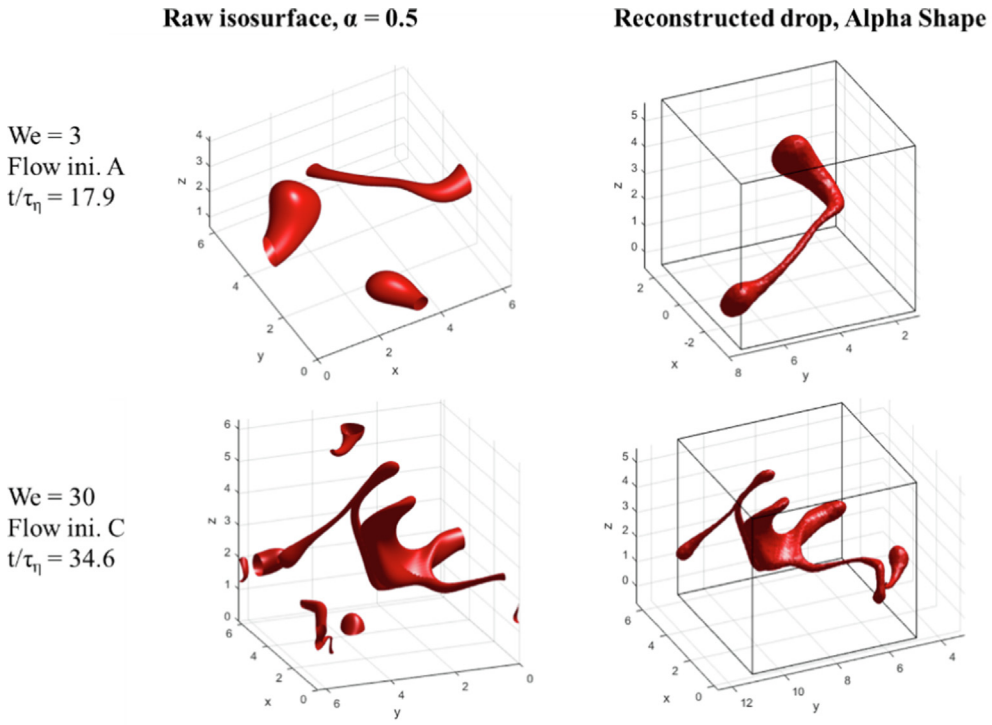

Fig. A1. Comparison between raw VOF-isosurfaces (left) and reconstructed drops (right). The first row shows a case of low deformation complexity (We = 3, flow realization A, t/τ_η = 17.9) and the second row shows a case of a more complex deformation (We = 30, flow realization C, t/τ_η = 34.6).

to correct this, in order not to adversely influence the morphological representation.

References

Alopaeus, V., 2022. Modeling surfactant and drop size dynamics in polydisperse liquid-liquid systems with population balances. Chem. Eng. Sci. 248. https://doi.org/10.1016/j.ces.2021.117269 117269.

Andersson, R., Andersson, B., 2006. Modeling the breakup of fluid particles in turbulent flows. AIChE J. 52 (6), 2031–2038.

Andersson, R., Helmi, A., 2014. Computational fluid dynamics simulation of fluid particle fragmentation in turbulent flows. Appl. Math. Model. 38 (17–18), 4186–4196. https://doi.org/10.1016/j.apm.2014.01.005.

Arai, K., Konno, M., Mutunaga, Y., Saito, S., 1977. Effect of dispersed-phase viscosity on the maximum stable drop size for breakup in turbulent flow. J. Chem. Eng. Jpn. 10, 325–330. https://doi.org/10.1252/JCEJ.10.325.

Ashar, M., Arlov, D., Carlsson, F., Innings, F., Andersson, R., 2018. Single droplet breakup in a rotor-stator mixer. Chem. Eng. Sci. 181, 186–198. https://doi.org/10.1016/j.ces.2018.02.021.

Attaie, R., Richter, R.L., 2000. Size Distribution of Fat Globules in Goat Milk. J. Dairy Sci. 83, 940–944. https://doi.org/10.3168/jds.S0022-0302(00)74957-5.

Bałdyga, J., Podgorska, W., 1998. Drop break-up in intermittent turbulence: Maximum stable and transient sizes of drops. The Canadian Journal of Chemical Engineering 76, 456–470. https://doi.org/10.1002/cjce.5450760316.

Bisten, A., Schuchmann, H.P., 2016. Optical measuring methods for the investigation of high-pressure homogenisation. Processes 4 (4), 41. https://doi.org/10.3390/pr4040041.

Calabrese, R.V., Chang, T.P.K., Dang, P.T., 1986. Drop breakup in turbulent stirred-tank contactors. Part I: Effect of dispersed-phase viscosity. AIChE J. 32 (4), 657–666. https://doi.org/10.1002/aic.690320416.

Costa, P. (2018). A FFT-based finite-difference solver for massively-parallel direct numerical simulations of turbulent flows. Computers and Mathematics with Applications 76 (8), 1853–1862, arXiv: arXiv:1802.10323v3.

Crialesi-Esposito, M., Rosti, M.E., Chibbaro, S., Brandt, L. (2021). Modulation of homogeneous and isotropic turbulence in emulsions. Manuscript. arXiv:2108.08722 [physics.flu-dyn].

Davies, J.T., 1985. Drop sizes of emulsions related to turbulent energy dissipation rates. Chem. Eng. Sci. 40, 839–842. https://doi.org/10.1016/0009-2509(85)85036-3.

Di Marzo, L., Cree, P., Barbano, D.M., 2016. Prediction of fat globule particle size in homogenized milk using Fourier transform mid-infrared spectra. J. Dairy Sci. 99, 8849–18560. https://doi.org/10.3168/jds.2016-11284.

Eastwood, C.D., Armi, L., Lasheras, J.C., 2004. The breakup of immiscible fluids in turbulent flows. J. Fluid Mech. 502, 309–333. https://doi.org/10.1017/S0022112003007730.

Edelsbrunner, H., Kirkpatrick, D.G., Seidel, R., 1983. On the shape of a set of points in the plane. IEEE Trans. Inf. Theory 29 (4), 551–559. https://doi.org/10.1109/TIT.1983.1056714.

Elghobashi, S., 2019. Direct numerical simulation of turbulent flows laden with droplets or bubbles. Annu. Rev. Fluid Mech. 51, 217–244. https://doi.org/10.1146/annurev-fluid-010518-040401.

Eswaran, V., Pope, S.B., 1988. An examination of forcing in direct numerical simulations of turbulence. Comput. Fluids 16, 257–278. https://doi.org/10.1016/0045-7930(88)90013-8.

Galinat, S., Garrido Torres, L., Masbernat, O., Guiraud, P., Risso, F., Dalmazzone, C., Noik, C., 2007. Breakup of a drop in a liquid-liquid pipe flow through an orifice. AIChE J. 53 (1), 56–68.

Ghasempour, F., Andersson, R., Andersson, B., 2015. Identification and characterization of three-dimensional turbulent flow structures. AIChE J. 62, 1265–1277. https://doi.org/10.1002/aic.15085.

Guo, Z., Fletcher, D.F., Haynes, B.S., 2014. A Review of computational modelling of flow boiling in microchannel. J. Computational Multiphase Flows 6, 79–110. https://doi.org/10.1260/1757-482X.6.2.79.

Håkansson, A., 2021. The role of stochastic time-variations in turbulent stresses when predicting drop breakup – a review of modelling approaches. Processes 9, 1904. https://doi.org/10.3390/pr9111904.

Håkansson, A., Trägårdh, C., Bergenståhl, B., 2009. Dynamic simulation of emulsion formation in a high pressure homogenizer. Chem. Eng. Sci. 64, 2915–2925. https://doi.org/10.1016/j.ces.2009.03.034.

Håkansson, A., Fuchs, L., Innings, F., Revstedt, J., Trägårdh, C., Bergenståhl, B., 2011. High resolution experimental measurement of turbulent flow field in a high pressure homogenizer model its implication on turbulent drop fragmentation. Chem. Eng. Sci. 66, 1790–1801. https://doi.org/10.1016/j.ces.2011.01.026.

Håkansson, A., 2016. Scale-down failed – Dissimilarities between high-pressure homogenizers of different scales due to failed mechanistic matching. J. Food Eng. 195, 31–39. https://doi.org/10.1016/j.jfoodeng.2016.09.019.

Håkansson, A., 2018. An experimental investigation of the probability distribution of turbulent fragmenting stresses in a high-pressure homogenizer. Chem. Eng. Sci. 177, 139–150. https://doi.org/10.1016/j.ces.2017.11.045.

Håkansson, A., 2019. Emulsion formation by homogenization: Current understanding and future perspectives. Annual Rev. Food Sci. Technology 10, 239–258. https://doi.org/10.1146/annurev-food-032818-121501.

Håkansson, A., 2020. Experimental methods for measuring the breakup frequency in turbulent emulsification: A critical review. ChemEngineering 4, 52. https://doi.org/10.3390/chemengineering4030052.

Haller, G., 2005. An objective definition of a vortex. J. Fluid Mech. 525, 1–26. https://doi.org/10.1017/S0022112004002526.

Herø, E.H., La Forgia, N., Solsvik, J., Jakobsen, H.A., 2020. Single drop breakage in turbulent flow: Statistical data analysis. Chem. Eng. Sci. X 8, 100082.

Hinze, J.O., 1955. Fundamentals of the hydrodynamic mechanism of splitting in dispersion process. AIChE J. 1, 289–295. https://doi.org/10.1002/aic.690010303.

Hunt, J.C.R., Wray, A. A., Moin, P. (1988). Eddies, streams, and convergence zones in turbulent flows. Proceedings of the Summer Program (Center for Turbulence Research, 1988), pp. 193–208.
Ii, S., Xie, B., Xiao, F., 2014. An interface capturing method with a continuous function: The THINC method on unstructured triangular and tetrahedral meshes. J. Comput. Phys. 259, 260–269. https://doi.org/10.1016/j.jcp.2013.11.034.
Innings, F., Trägårdh, C., 2007. Analysis of the flow field in a high-pressure homogenizer. Exp. Therm Fluid Sci. 32, 345–354. https://doi.org/10.1016/j.expthermflusci.2007.04.007.
Innings, F., Fuchs, L., Trägårdh, C., 2011. Theoretical and experimental analyses of drop deformation and break-up in a scale model of a high-pressure homogenizer. J. Food Eng. 103, 21–28. https://doi.org/10.1016/j.jfoodeng.2010.09.016.
Karimi, M., Andersson, R., 2019. Dual mechanism model for fluid particle breakup in the entire turbuent spectrum. AIChE J. 65, (8). https://doi.org/10.1002/aic.16600 e16600.
Kelemen, K., Gepperth, S., Koch, R., Bauer, H.J., Schuchmann, H.P., 2015. On the visualization of droplet deformation and breakup during high-pressure homogenization. Microfluid. Nanofluid. 19, 1139–1158. https://doi.org/10.1007/s10404-015-1631-z.
Kessler, H.G., 2002. Food and Bio Process Engineering: Dairy Technology. Verlag A, Kessler, Munich, Germany.
Kolmogorov, A.N. (1949). On the breakage of drops in a turbulent flow. Dokl. Akad. Nauk. SSSR 66, 825-828. (Originally in Russian. Reprinted and translated in Selected Works of A.N. Kolmogorov, Volume 1: Mathematics and Mechanics, Tikhomirov, V.M. (ed.), 1991, p.339-343).
Komrakova, A.E., 2019. Single drop breakup in turbulent flow. Canadian J. Chemical Engineering 97, 2727–2739. https://doi.org/10.1002/cjce.23478.
Komrakova, A.E., Eskin, D., Derksen, J.J., 2015. Numerical study of turbulent liquid-liquid dispersions. AIChE J. 61, 2618–2633. https://doi.org/10.1002/aic.14821.
Kulkarni, V., Sojka, P.E. (2014). Bag breakup of low viscosity drops in the presence of a continuous air jet. Physics of Fluids 26, 072103. DOI: 10.1063/1.4887817.
Lalanne, B., Masbernat, O., Risso, F., 2019. A Model for drop and bubble breakup frequency based on turbulence spectra. AIChE J. 65, 347–359. https://doi.org/10.1002/aic.16374.
Maaß, S., Kraume, M., 2012. Determination of breakage rates using single drop experiments. Chem. Eng. Sci. 70, 146–164. https://doi.org/10.1016/j.ces.2011.08.027.
Martínez-Bazán, C., Montañés, J.L., Lasheras, J.C., 1999. On the breakup of an air bubble injected into a fully developed turbulent flow. Part 1. Breakup frequency. J. Fluid Mech. 401, 157–182. https://doi.org/10.1017/S0022112099006680.
Masuk, A.U.M., Salibindla, A.K.R., Ni, R., 2021. Simultaneous measurements of deforming Hinze-scale bubbles with surrounding turbulence. J. Fluid Mech. 910, A21. https://doi.org/10.1017/jfm.2020.933.
McClements, D.J., 2016. Food emulsions: principles, practices, and techniques. CRC Press, Boca Raton, FL.
Miller, C.A., Scriven, L.E., 1968. The oscillations of a fluid droplet immersed in another fluid. J. Fluid Mech. 32, 417–435. https://doi.org/10.1017/S0022112068000832.
Mininni, P.D., Alexakis, A., Pouquet, A., 2006. Large-scale flow effects, energy transfer, and self-similarity on turbulence. Phys. Rev. E 74. https://doi.org/10.1103/PhysRevE.74.016303 016303.
Mohr, K., 1987. High-pressure homogenization. Part I. Liquid-liquid dispersion in turbulence fields of high energy density. J. Food Eng. 6, 177–186. https://doi.org/10.1016/0260-8774(87)90023-9.
Mukherjee, S., Safdari, A., Shardt, O., Kenjeres, S., Van den Akker, H.E.A., 2019. Droplet–turbulence interactions and quasi-equilibrium dynamics in turbulent emulsions. J. Fluid Mech. 878, 221–276. https://doi.org/10.1017/jfm.2019.654.
Mutsch, B., Preiss, F.J., Dagenbach, T., Karbstein, H.P., Kähler, C.J., 2021. Scaling of droplet breakup in high-pressure homogenizer orifices. Part ii: Visualization of the turbulent droplet breakup. ChemEngineering 5, 7. https://doi.org/10.3390/chemengineering5010007.
Olad, P., Cialesi, M., Brandt, L., Innings, F., Håkansson, A., 2021. A DNS investigation of the one-phase flow in an emulsification device. J. Fluid Engineering.
Olad, P., Innings, F., Håkansson, A. (2021b). Stochastic time-variations in the dissipation rate of turbulent kinetic energy in an emulsification device – insights from numerical experiments. Submitted to journal.
Olad, P., Innings, F., Håkansson, A. (2021c). An empirical investigation of the second-order structure functions in an emulsification device with relevance for fragmentation frequency modelling approaches. Submitted to journal.
Phipps, L.W., 1975. The fragmentation of oil drops in emulsion by a high-pressure homogenizer. J. Phys. D Appl. Phys. 8, 448–462. https://doi.org/10.1088/0022-3727/8/4/018.
Phipps, L.W., 1985. The high pressure dairy homogenizer. The National Institute for Research in Dairying, Reading, UK.
Podvigina, O., Pouquet, A. (1994). On the non-linear stability of the 1:1:1 ABC flow. Physica D: Nonlinear Phenomena 75 (4), 471–508. DOI: 10.1016/0167-2789(94)00031-X.
Pope, S.B., 2000. Turbulent flows. Cambridge University Press, Cambridge, UK.
Preiss, F.J., Mutsch, B., Kähler, C.J., Karbstein, H.P., 2021. Scaling of Droplet Breakup in High-Pressure Homogenizer Orifices. Part I: Comparison of Velocity Profiles in Scaled Coaxial Orifices. ChemEngineering 5 (1), 7. https://doi.org/10.3390/chemengineering5010007.
Qian, D., McLaughlin, J.B., Sankaranarayanan, K., Sundaresan, S., Kontomaris, K., 2006. Simulation of bubble breakup dynamics in homogenous turbulence. Chem. Eng. Commun. 193, 1038–1063. https://doi.org/10.1080/00986440500354275.
Ransmark, E., Svensson, E., Svedberg, I., Göransson, A., Skoglund, T., 2019. Measurement of homogenisation efficiency of milk by laser diffraction and centrifugation. Int. Dairy J. 96, 93–97. https://doi.org/10.1016/j.idairyj.2019.04.011.
Risso, F., Fabre, J., 1998. Oscillations and breakup of a bubble immersed in a turbulent field. J. Fluid Mech. 372, 323–355. https://doi.org/10.1017/S0022112098002705.
Rivière, A., Mostert, W., Perrard, S., Deike, L., 2021. Sub-Hinze scale bubble production in turbulent bubble break-up. J. Fluid Mech. 917, A40. https://doi.org/10.1017/jfm.2021.243.
Rosti, M.E., De Vita, F., Brandt, L., 2019. Numerical simulations of emulsions in shear flows. Acta Mech. 230 (2), 667–682. https://doi.org/10.1007/s00707-018-2265-5.
Scarbolo, L., Bianco, F., Soldati, A. (2015). Coalescence and breakup of large droplets in turbulent channel flow. Physics of Fluids 27, 073302. DOI: 10.1063/1.4923424.
Schultz, S., Wagner, G., Urban, K., Ulrich, J. (2004). High-pressure homogenization as a process for emulsification. Chemical Engineering & Technology 27(4), :361–368. DOI: 10.1002/ceat.200406111.
Shao, C., Luo, K., Yang, Y., Fan, J., 2018. Direct numerical simulation of droplet breakup in homogeneous isotropic turbulence: The effect of the Weber number. Int. J. Multiph. Flow 107, 263–274. https://doi.org/10.1016/j.ijmultiphaseflow.2018.06.009.
Shinnar, R., 1961. On the behaviour of liquid dispersions in mixing vessels. J. Fluid Mech. 10 (2), 259–275. https://doi.org/10.1017/S0022112061000214.
Singh, R.P. (2007). Heating and cooling processes for foods. In: Handbook of Food Engineering, 2nd ed. Eds. D.R. Heldman, D.B. Lund, CRC Press, Boca Raton, FL.
Skartlien, R., Sollum, E., Schumann, H. (2013). Droplet size distributions in turbulent emulsions: Breakup criteria and surfactant effects from direct numerical simulations. The Journal of Chemical Physics 139, 174901. DOI: 10.1063/1.4827025.
Soh, G.Y., Yeoh, G.H., Timchenko, V., 2016. An algorithm to calculate interfacial area for multiphase mass transfer through the volume-of-fluid method. Int. J. Heat Mass Transf. 100, 573–581. https://doi.org/10.1016/j.ijheatmasstransfer.2016.05.006.
Solsvik, J., Jakobsen, H.A., 2015. Single drop breakup experiments in stirred liquid-liquid tank. Chem. Eng. Sci. 131, 219–234. https://doi.org/10.1016/j.ces.2015.03.059.
Solsvik, J., Jakobsen, H.A., 2016. A review of the statistical turbulence theory required extending the population balance closure models to the entire spectrum of turbulence. AIChE J. 62 (5), 1795–1820. https://doi.org/10.1002/aic.15128.
Solsvik, J., Maaß, S., Jakobsen, H.A., 2016. Definition of the single drop breakup event. Ind. Eng. Chem. Res. 55 (10), 2872–2882. https://doi.org/10.1021/acs.iecr.6b00591.
Soni, S.K., Kirar, P.K., Kolhe, P., Sahu, K.C., 2020. Deformation and breakup of droplets in an oblique continuous air stream. Int. J. Multiph. Flow 122. https://doi.org/10.1016/j.ijmultiphaseflow.2019.103141 103141.
Tadros, T.F. (2013). Emulsion Formation and Stability. Wiley-VCH, Weinheim, Germany.
Tcholakova, S., Lesov, I., Golemanov, K., Denkov, N.D., Judat, S., Engel, R., Danner, T., 2011. Efficient emulsification of viscous oils at high drop volume fraction. Langmuir 27, 14783–14796. https://doi.org/10.1021/la203474b.
Tcholakova, S., Vankova, N., Denkov, N.D., Danner, T., 2007. Emulsification in turbulent flow: 3. Daughter drop-size distribution. J. Colloid Interface Sci. 310, 570–589. https://doi.org/10.1016/j.jcis.2007.01.097.
Vallefuoco, D., Naso, A., Godeferd, F.S., 2018. Small-scale anisotropy induced by spectral forcing and by rotation in non-helical and helical turbulence. J. Turbul. 19 (2), 107–140. https://doi.org/10.1080/14685248.2017.1400667.
Vankova, N., Tcholakova, S., Denkov, N.D., Ivanov, I., Vulchev, V.D., Danner, T., 2007. Emulsification in turbulent flow 1. Mean and maximum drop diameters in inertial and viscous regimes. J. Colloid Interface Sci. 312, 363–380. https://doi.org/10.1016/j.jcis.2007.03.059.
Vejražka, J., Zedníková, M., Stranovský, P., 2018. Experiments on breakup of bubbles in a turbulent flow. AIChE J. 64, 740–757. https://doi.org/10.1002/aic.15935.
Vela-Martín, A., Avila, M., 2021. Deformation of drops by outer eddies in turbulence. J. Fluid Mech. 929, A38. https://doi.org/10.1017/jfm.2021.879.
Zhou, H., Yu, X., Wang, B., Jing, S., Lan, E., Li, S., 2021. Modeling study on drop breakup time in turbulent dispersions. Chem. Eng. Sci. 238. https://doi.org/10.1016/j.ces.2021.116599 116599.